Volume 6 Number 1 March 2017

STUDENT JOURNAL OF PHYSICS

INDIAN ASSOCIATION OF PHYSICS TEACHERS

ISSN – 2319-3166

STUDENT JOURNAL OF PHYSICS

EDITORIAL BOARD

Editor in Chief

L. Satpathy, Institute of Physics, Bhubaneswar, India (satpathy@iopb.res.in)

Chief Editors

S. D. Mahanti, Physics and Astronomy Department, Michigan State University, East Lansing, Mi 48824, USA (mahanti@pa.msu.edu)

A.M. Srivastava, Institute of Physics, Bhubaneswar, India (ajit@iopb.res.in)

INTERNATIONAL EDITORIAL BOARD

Danny Caballero, Department of Physics, Michigan State University, U.S.A. (caballero@pa.msu.edu)

Gerd Kortemeyer, Joint Professor in Physics & Lyman Briggs College, Michigan State University, U.S.A. (kortemey@msu.edu)

Bedanga Das Mohanty, NISER, Bhubaneswar, India (bedanga@niser.ac.in)

Prasanta Panigrahi, IISER, Kolkata, India (panigrahi.iiser@gmail.com)

K.C. Ajith Prasad, Mahatma Gandhi College, Thiruvananthapuram, India (ajithprasadkc@gmail.com)

Ralph Scheicher, Physics Department, University of Uppsala, Sweden (ralph.scheicher@physics.uu.se)

Vijay A. Singh, Homi Bhabha Centre for Science Education (TIFR), Mumbai, India (physics.sutra@gmail.com)

Allison Walker, Department of Physics, University of Bath Bath BA2 7AY, UK (A.B.Walker@bath.ac.uk)

INTERNATIONAL ADVISORY BOARD

H.S. Mani, CMI, Chennai, India (hsmani@cmi.ac.in)

S. M. Moszkowski, UCLA, USA (stevemos@ucla.edu)

Jogesh C. Pati, SLAC, Stanford, USA (pati@slac.stanford.edu)

Satya Prakash, Panjab University, Chandigarh, India (profsprakash@hotmail.com)

T.V. Ramakrishnan, BHU, Varanasi, India (tvrama@bhu.ac.in)

D. P. Roy, Homi Bhabha Centre for Science Education (TIFR), Mumbai, India (dproy1@gmail.com)

Ashoke Sen, HRI, Allahabad, India (sen@hri.res.in)

X. Vinas, Departament d’Estructura i Constituents de la Mat`eria and Institut de Ci`encies del Cosmos, Facultat de F ´ısica, Universitat de Barcelona, Barcelona, Spain (xavier@ecm.ub.edu)

Technical Editor

D. Pradhan, ILS, Bhubaneswar, India (dayanidhi.pradhan@gmail.com)

Web Management

Aditya Prasad Ghosh, IOP, Bhubaneswar, India (aditya@iopb.res.in)

Registered Office

Editor in Chief, SJP, Institute of Physics, Sainik School,
Bhubaneswar, Odisha, India - 751005

STUDENT JOURNAL OF PHYSICS

Scope of the Journal

The journal is devoted to research carried out by students at undergraduate level. It provides a platform for the young students to explore their creativity, originality, and independence in terms of research articles which may be written in collaboration with senior scientist(s), but with a very significant contribution from the student. The articles will be judged for suitability of publication in the following two broad categories:

1. **Project based articles**
   These articles are based on research projects assigned and guided by senior scientist(s) and carried out predominantly or entirely by the student.
2. **Articles based on original ideas of student**
   These articles are originated by the student and developed by him/ her with possible help from senior advisor.

   Very often an undergraduate student producing original idea is unable to find a venue for its expression where it can get due attention. SJP, with its primary goal of encouraging original research at the undergraduate level provides a platform for bringing out such research works.

   It is an online journal with no cost to the author.

Since SJP is concerned with undergraduate physics education, it will occasionally also publish articles on science education written by senior physicists.

Information for Authors

- Check the accuracy of your references.
- Include the complete source information for any references cited in the abstract. (Do not cite reference numbers in the abstract.)
- Number references in text consecutively, starting with [1].
- Language: Papers should have a clear presentation written in good English. Use a spell checker.

Submission

1. Use the link "Submit" of Website to submit all files (manuscript and figures) together in the submission (either as a single .tar file or as multiple files)
2. Choose one of the Editors in the link "Submit" of Website as communicating editor while submitting your manuscript.

Preparation for Submission

Use the template available at "Submit" section of Website for preparation of the manuscript.

Re-Submission

- For re-submission, please respond to the major points of the criticism raised by the referees.
- If your paper is accepted, please check the proofs carefully.

Scope

- SJP covers all areas of applied, fundamental, and interdisciplinary physics research.

Editorial

The current trend in Undergraduate Physics education in many countries is marked with emphasis on the cultivation of innovation and creativity amongst the students through the promotion of research culture. USA has the program called REU i.e Research Experience for Undergraduates under which UG students visit national laboratories and universities during summer months to carry out research under the guidance of the inhouse scientists. India has a similar program called NIUS i.e National Initiative in Undergraduate Science. Other countries do have similar programs. Also, at any time, students, even at undergraduate level, keep coming with new ideas and calculations. Even when such works are creative and original, due to their limited scope, it is often difficult to publish these in standard research journals. To provide a platform to bring out this wide variety of creative research carried out by undergraduate students, there is a need for an appropriate international journal. Herewith we are happy to present such a forum, which we hope with cooperation and support from the concerned international community of students and teachers, will be able to serve the above need adequately.

Student Journal of Physics presented here is not a completely new journal. It originally started in 2004 in India under the auspicies of the Indian Association of Physics Teachers (IAPT) with title PRAYAS: Students Journal of Physics with the objective of inculcating the spirit of research amongst the undergraduate students (upto M.Sc. level) of Indian universities. It got its recognition as a viable journal of substantial value and importance in 2012 when it got its international registration number ISSN 2319-3166 with a new title Student Journal of Physics - a better universal title without flavor of any nation or region. In its short life span of 13 years, it has undoubtedly spread awareness of the importance of innovation and research in undergraduate education partly manifested in the enthausiastic participation of large number of students in the newly created National Student Symposium on Physics being held annually since 2013.

The success of the above experiment has inspired us to enhance SJP potential by fully converting it into an international journal with active participation of students and scientists from other countries retaining the same title and Regd. Number. This new avatar of SJP commences its publication with the present issue. It has a new International Editorial Board and International Advisory Body comprising members from several countries, which will be expanded in the course of its journey. It will be an on-line journal, free of any cost to the authors, and freely available worldwide in internet.

SJP provides a platform for the undergraduate students to explore their creativity, originality and independence in terms of research articles, which may be written in collaboration with senior scientist(s), but with a very significant contribution from the student. The articles will be judged for suitability of publication in the following two broad categories:

1. **Project based articles**
   These articles are based on research projects assigned and guided by senior scientist(s) and carried out predominantly or entirely by the student.

2. **Articles based on original ideas of student**
   These articles are originated by the student and developed by him/ her with possible help from senior advisor. Very often an undergraduate student producing original idea is unable to find a venue for its expression where it can get due attention. SJP will address it with due seriousness.

Since SJP is concerned with undegraduate physics education, it will occassionally publish articles on education written by senior physicists.

L. Satpathy

STUDENT JOURNAL OF PHYSICS

Taking A Scientific Approach To Physics Education

Marcos D. Caballero
Department of Physics and Astronomy & CREATE for STEM Institute Michigan State University, East Lansing, MI, USA 48824.

Keywords. Physics education, Undergraduate research.

As physicists, we are taught very early of the debate about the geocentric solar system. The arguments that included physics, philosophy, and religion firmly planted the Ptolemaic model of the universe as the standard. A simpler model by Copernicus led us to understand the heliocentric solar system and explain the paradoxical retrograde motion of Mars. As we became more sophisticated in our observations and mathematical tools, our understanding of what held the heavens in place was replaced as observations by Kepler, Brahe, and Galileo were explained by the physics and mathematics developed by Newton and Leibniz. As we struggled to understand why light bent around astronomical objects, why we could never predict Mercurys orbit accurately, whether we were at the center of the universe or not, why tiny alpha particles bounced off massive gold foil, and how it was possible for an electron to be everywhere and yet nowhere, we developed new physics thanks to Einstein, Hubble, Wheeler, Schroedinger, Dirac, Wigner, Pauli, Curie, Thompson, Heisenberg and many, many others to better predict and to more readily explain our universe and everything in it. As we continue to expand out, testing the limits of physics, we begin to understand that we truly know nothing about our universe and the best we can hope to do is make models that explain our latest observations and make predictions about new ones. This is both the beauty and the challenge of physics: we are never done and we never want to be done. There is always something more to explain, something to understand more deeply. Modern physics research leverages experimental, theoretical, and computational techniques to develop models and explanations of the natural world - and we do that quite well.

But what of how people come to understand physics? How do people know physics? How do people learn physics? How do we help people to learn physics better and more deeply? How do we help people develop an understanding that has taken millennia to construct? That is my job. I am a physicist who studies how people learn and I work to improve the conditions under which that learning occurs. Rather than going by feel, I take a scientific approach to physics education. I also use experimental, theoretical, and computational techniques in my work, but I develop models and explanations of how people learn about the physical world rather than learning about the world itself. The field in which I work is called Physics Education Research (PER). And what we do, we also do quite well.

By comparison to most subfields on physics, PER is a relatively new field truly starting with the early work by Arnold Arons, Robert Karplus, Lillian McDermott, and others about 40 years ago

[1-3]. Much of this early research and some current work, including research I have done myself[4-7], is more akin to applied physics. That is, instead of trying to explain the observed phenomena (e.g., how do students think about buoyancy from a variety of perspectives), we have (historically) attempted to engineer a solution to the problem (e.g., how do we make students think about buoyancy correctly). This applied lens has served the physics community very well. In the last 40 years, PER has consistently demonstrated a number of core principles of instruction at the undergraduate level [8,9]:

- Students learn physics by engaging with course material actively and cooperatively.
- Students learn physics by experiencing physics in authentic ways that align with their interests.
- Student learning in physics is best supported by a community that respects student ideas and experiences.

These principles seem to be fairly strong and consistent predictors of overall student success within a given topic or a given course [10]. In fact, these general principles appear to apply to many disciplines [11].

While this research has assisted us greatly in understanding how to help students learn physics as it is taught presently, our discoveries have pressed us to answer new questions, for example:

- What is the nature of student understanding in physics, and what experiences bring students to that understanding?
- How do students participate in physics and how does that participation shape their future with physics?
- What effects do new technology, pedagogy, curriculum, and teaching practices have on student understanding and engagement in physics?
- How do we broaden participation in physics to include and support students from groups who are historically underrepresented in physics (i.e., women and students of color)?

To answer these new questions, PER has had to evolve. Our field is more interdisciplinary than before, we leverage the work of educational researchers and social scientists outside of our field, much in the way that biophysicists leverage understanding from biology. Our field makes use of theories, methods, and tools from fields such as science education research, educational psychology, sociology, anthropology, and the fields of women and race studies. We are more grounded in the history, tradition, and culture of educational research than the early years. We are gaining stronger and more complete evidence on student learning than before. Our field has matured and developed in ways that are helping to strengthen the research, but still maintain relevance and importance to the physics community. A summary of the birth and evolution of the field of PER was commissioned by the National Research Council and published recently [10].

But I digress. My own work concerns two areas of understanding in physics: (1) mathematics and (2) scientific computing. Both areas of research attempt to answer broad questions:

- What does student engagement in mathematics/scientific computing in physics look like?
- How can we promote stronger engagement?
- How do students come to understand physics through mathematics/scientific computing and vice versa?
- How do students come to understand how to use mathematics/scientific computing to do physics work?
- What are the different experiences with mathematics/scientific computing that shape students relationship with physics?

Each of these questions is quite broad and research projects that support answering those questions is part of what the Physics Education Research Lab at Michigan State University ($http://perl.pa.msu.edu$), which I help direct, does. We have a number of projects in different areas, but here I will highlight only two.

The first project aims to make sense of how students develop their understanding of scientific computing over time. This work has developed out of my prior work to incorporate and to study students use of scientific computing in introductory and upper-level physics courses [7,12,13]. This project leverages variation theory [14] through the use of narrations of students prior experiences in the classroom. We aim to build claims about the different ways in which students working in small groups understand the Python code they write in an introductory physics course and how that understanding changes over the first four weeks of the course (when much of the instruction on scientific computing occurs). Several students taking this introductory physics course where they model physical systems with the Python programming language are interviewed each week.

In each weekly interview, students are presented with the code they had written in class during the previous week. They are asked to discuss what the different lines of code mean and how they came to develop those lines of code in their group. Through this interview and the subsequent discussion about specific features of their code, we develop our own understanding of the different ways students come to write the programs in their course. A final interview (not yet conducted) will ask students to reflect on specific instances when parts of their code were written and what their (and their groups) thinking was at the time. This reflective interview will make use of in-class video recordings where students are discussing with their group mates how to develop and to write the program for that day.

In a second project, we are trying to understand how students come to use sophisticated mathematical tools (such as multivariable integration and vector decomposition in different coordinate systems) facilely. This work stems from my prior research on students use of mathematics in upper-level physics courses [6,15-20]. This second project leverages Resource theory [21-24] and a dyad interview methodology where students explain their approaches to and decisions around solving mathematically-intensive upper-level physics problems to each other. The interviewer takes the approach of encouraging students to discuss together what the students think the proper approach should be.

The point of this research effort is not to judge students solutions as correct or incorrect nor to judge the path they develop to their solution as appropriate or not, but rather to observe the multitude of ways that students approach using mathematics on these problems. Our aim is to develop an understanding of not only what students do when confronted with these kinds of problems, but also why students choose to do what they do. That is, what prior experiences or in-the-moment decisions lead them to solve a particular problem in the way that they did. As a cross-sectional study (one that looks across the physics curriculum from first-year to fourth year), we further aim to understand how those approaches change over time and are influenced by the experiences in more advanced physics courses that students take later.

While there are a number of other studies and research endeavors that our lab is engaged in, I believe these two examples provide concrete illustrations of the approach to physics education that current researchers of undergraduate physics teaching and learning are beginning to take. Ours is an endeavor to understand how students come to learn physics and what promotes different kinds of learning in our physics classrooms.

I will end as I began speaking about evolving models. What we know now about student learning in physics, what models are prevalent and useful, and what tools that provide insight are only as good as the phenomenon they can explain. As researchers develop deeper understanding of student learning, as we ask and answer new questions about how that understanding develops, we must evolve our theories, models, and methods to investigate new phenomena. It is by asking these new questions, testing new models, and developing new research studies that build off prior work that we take a scientific approach to physics education.

1. ACKNOWLEDGEMENTS

I would like to acknowledge the work of my collaborators on the projects presented here, in alphabetical order: Leanne Doughty, Paul W. Irving, Matthew A. Kohlmyer, Michael J. Obsniuk, Rachel E. Pepper, Steven J. Pollock, Michael F. Schatz, Daniel A. Rehn, Anna Turnbull, Bethany R. Wilcox, and Steven Wolf. I would also like to thank the generous support for this research from the University of Colorados Science Education Initiative, the National Science Foundations Division of Undergraduate Education, and the CREATE for STEM Institute at Michigan State University.

References

[1] A. B. Arons, Am. J. Phys. 44, 834 (1976).
[2] A. B. Arons and R. Karplus, Am. J. Phys. 44, 396 (1976).
[3] D. E. Trowbridge and L. C. McDermott, Am. J. Phys. 48, 1020 (1980).

[4] M. D. Caballero, E. F. Greco, E. R. Murray, K. R. Bujak, M. Jackson Marr, R. Catrambone, M. A. Kohlmyer, and M. F. Schatz, Am. J. Phys. 80, 638 (2012).

[5] M. Kohlmyer, M. Caballero, R. Catrambone, R. Chabay, L. Ding, M. Haugan, M. Marr, B. Sherwood, and M. Schatz, Phys. Rev. ST Phys. Educ. Res 5, (2009).

[6] B. R. Wilcox, M. D. Caballero, D. A. Rehn, and S. J. Pollock, Phys. Rev. ST Phys. Educ. Res 9, 020119 (2013).

[7] M. Caballero, M. Kohlmyer, and M. Schatz, Phys. Rev. ST Phys. Educ. Res 8, 020106 (2012).

[8] D. E. Meltzer and R. K. Thornton, Am. J. Phys. 80, 478 (2012).

[9] L. C. McDermott and E. F. Redish, Am. J. Phys. 67, 755 (1999).

[10] National Research Council, Adapting to a Changing World–Challenges and Opportunities in Undergraduate Physics Education (National Academies Press, 2013).

[11] National Research Council, Discipline-Based Education Research (National Academies Press, 2012).

[12] M. D. Caballero and S. J. Pollock, Am. J. Phys. 82, 231 (2014).

[13] M. J. Obsniuk, P. W. Irving, and M. D. Caballero, in 2015 Physics Education Research Conference (American Association of Physics Teachers, 2015), pp. 239242.

[14] Encyclopedia of the Sciences of Learning, edited by N. M. Seel (Springer US, Boston, MA, 2012), pp. 323323.

[15] M. D. Caballero, B. R. Wilcox, R. E. Pepper, and S. J. Pollock, in 2012 Physics Education Research Conference (American Association of Physics Teachers, 2013), pp. 90-93.

[16] B. R. Wilcox, M. D. Caballero, R. E. Pepper, and S. J. Pollock, in 2012 Physics Education Research Conference (American Association of Physics Teachers, 2013) pp. 418-421.

[17] M. D. Caballero and S. J. Pollock, in 2013 Physics Education Research Conference (American Association of Physics Teachers, 2014), pp. 8184.

[18] L. Doughty and M. D. Caballero, in 2014 Physics Education Research Conference (American Association of Physics Teachers, 2015), pp. 7174.

[19] A. Turnbull, L. Doughty, V. Sawtelle, and M. D. Caballero, in 2015 Physics Education Research Conference c (American Association of Physics Teachers, 2015), pp. 335338.

[20] S. F. Wolf, L. Doughty, P. W. Irving, E. C. Sayre, and M. D. Caballero, in 2014 Physics Education Research Conference (American Association of Physics Teachers, 2015), pp. 275278.

[21] D. Hammer, Am. J. Phys. 68, S52 (2000).

[22] D. Hammer, A. Elby, R. E. Scherr, and E. F. Redish, Transfer of Learning From a Modern Multidisciplinary Perspective 89 (2005).

[23] A. A. diSessa, Cognition and Instruction 10, 105 (1993).

[24] J. P. Smith III, A. A. diSessa, and J. Roschelle, The Journal of the Learning Sciences 3, 115 (1994).

.

STUDENT JOURNAL OF PHYSICS

Building of a Bakelite Resistive Plate Chamber Detector

Himangshu Neog
Final Year, Int. M.Sc., School of Physical Sciences National Institute of Science Education and Research Bhubaneswar, HBNI Jatni - 752050, India.

Abstract. A Bakelite Resistive Plate Chamber (RPC) has been fabricated using the facility available at NISER high energy physics laboratory using locally available materials. The semi-conductive graphite coatings on the outer surfaces of the electrodes are made and the surface resistivity of the graphite coatings are measured using a jig. The detector is leak tested using water manometer. The detail fabrication procedures and the results of surface resistivity measurement and leak test are presented in this article. Such detectors are used in high energy physics experiments, like for example the one proposed to detector neutrinos in Indian Neutrino Observatory.

Keywords. Resistive Plate Chamber, Particle detector.

1. INTRODUCTION

In recent times Resistive Plate Chambers (RPCs) are one of the most widely used detectors in high-energy physics (HEP) experiments. They are used mainly as triggering detectors to know that an event has occurred or as Time of Flight (TOF) detector [1]. The RPC is a gas filled detector utilizing a constant and uniform electric field produced between two parallel electrode plates made of a material with high bulk resistivity e.g. glass or Bakelite. RPC has good time resolution ($\sim 1 - 2ns$) and spatial resolution ($\sim$ cm). The high resistance of RPC plate limits the spark size produced after the ionization of gas due to the passing charged particles. I have carried out my first fabrication of such detectors at NISER using the facility available for imparting training at the undergraduate level to students. We have made a $30cm \times 30cm$ Bakelite resistive plate chamber module using locally available materials. Such detectors have been considered for the possibility of use in the high-energy physics experiments such as in India-based Neutrino Observatory program [2].

This paper discusses building of a RPC using Bakelite and other components from the local sources and the measurement of the surface resistivity of the detector. The detector is tested for gas leak. The method of leak test and the results are also presented.

2. CONSTRUCTION OF RPC

Two $30cm \times 30cm$ Bakelite sheets with $3mm$ thickness are used as electrodes. After proper cleaning with isopropyl alcohol, a graphite coating (surface resistivity $\sim$ a few hundreds of $k\Omega/\square$) is made on the outer surfaces of the RPC to distribute the applied voltage uniformly over the entire detector. A gap of $1cm$ from the edges to the graphite layer is maintained to avoid external sparking. The inner surfaces of the two sheets are separated by a $2mm$ gap. Uniform separation of the electrodes are ensured by using five button spacers of 1cm diameter and $2mm$ thickness, and edge spacers of $30cm \times 1cm \times 0.2 \sim cm$ dimension, both being made in the laboratory itself using a polycarbonate sheet. Two polycarbonate nozzles (1mm hole diameter in 2mm thickness) for gas inlet and outlet, are placed diagonally as part of the edge spacers. All the components of the RPC are shown in Fig. 1.

Figure 1. Various components for RPC fabrication. Two graphite coated bakelite sheets (A), edge spacers (B), gas nozzles (C) and pick-up strips (D).

All the spacers and nozzles are glued to the Bakelite sheets using Araldite epoxy adhesive. Finally the gas gap between two Bakelite sheets is made using the edge spacers and button spacers. Applying a layer of the epoxy adhesive to prevent permeation of moisture seals the edges of the Bakelite sheets. Two small copper tapes $\sim 20\mu m$ thick and $1cm \times 1cm$ are pasted by the kapton tape on both the outer surfaces (on the graphite coating side) for the application of high voltage. The high voltage connectors are soldered on these copper tapes. $100\mu m$ thick Mylar sheets are used on the two sides of the RPC to cover the graphite coatings and to isolate the graphite coated surface and the pick-up strips. The complete RPC module is shown in Fig.2.

In order to collect the accumulated induced charges, pick-up strips are placed above the graphite coated surfaces. The pick-up strips are made of aluminum, which are pasted on one side of 8 mm thick locally available foam. The area of each strip is 3cmx30cm with a separation of 2mm between two adjacent strips. The ground plane made of aluminum, is pasted on the other side of the foam.

Figure 2. Complete RPC module.

3. SURFACE RESISTIVITY MEASUREMENT

The surface resistivity of graphite coating that is one of the most important parameters for RPC is calculated by measuring the leakage current. This measurement is done with the help of a jig (developed locally) and a multimeter available in the laboratory. The jig is made of two 10cm long brass rods (conductor) separated by a 10cm long Teflon rod (insulator) and, connected in a square shape.

The working principle of the jig is that the resistance measured for a uniform thickness, t of graphite layer will give the surface resistivity of the graphite layer. The voltage is applied in the brass (conductor) through multimeter. If ρ is the bulk resistivity of the surface of length l and cross-sectional area A then the resistance is given by,

$$R = \rho l/A = \rho l/lt = \rho/t$$

So the surface resistivity depends only on the graphite material and the thickness of the graphite layer. Since the length of the metal rods and their separation is kept same the unit of the surface resistivity is given by $k\Omega/\Box$ and it reads $k\Omega$ per square. The uniformity of the surface resistivity of graphite coating for the two bakelite electrode plates is scanned moving the jig in horizontal and vertical direction on the graphite surface. For each direction 100 readings are taken. For each plate the uniformity is checked both in vertical and horizontal direction. The uniformity of the surface resistivity of a plate during horizontal measurement is shown in Fig. 3. For the plate 1 the average surface resistivity is found to be $\sim 500k\Omega/\Box$ and that for the plate 2 is found to be $\sim 800k\Omega/\Box$.

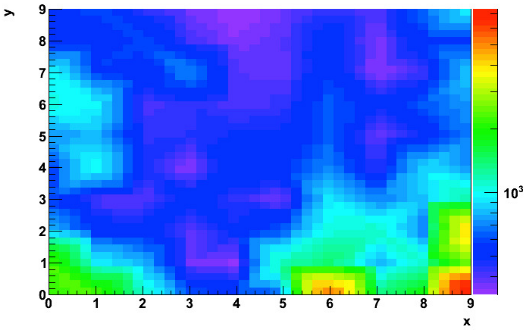

Figure 3. The surface resistivity in $k\Omega$ of graphite coated surface. x and y both dimensions are $30 \sim cm$ divided into $0-9$ zones.

4. LEAK TESTING

As a first step of building the detector it was subjected to a leak test by using a water manometry. The set-up for the leak testing is shown in Fig. 4. A U-tube filled with water is connected to the output of the RPC module and from the input argon gas is flown to the detector in such a way that there is a difference in the water level of the two arm of the U-tube. Once a difference is made the input of the detector is closed with a stop cork. The difference of the water level is measured with time. The measurement is continued for half an hour. The differential pressure in mbar is measured from the height difference of the water column. Initially the pressure decreases little bit but it remains constant at a differential pressure of 2 mbar during the measurement. The differential pressure as a function of the time is shown in Fig. 5.

Figure 4. Set-up for leak testing.

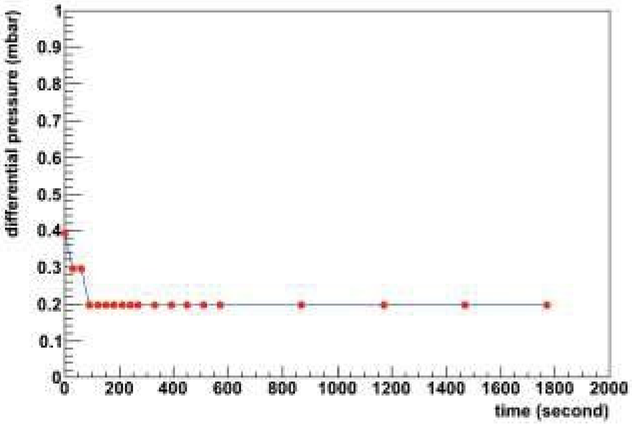

Figure 5. Pressure difference as a function of time.

5. CONCLUSION AND OUTLOOK

One RPC module is fabricated using Bakelite electrode. All the materials like Bakelite sheets, polycarbonate sheets, aluminum foils, foam, mylar sheets, copper tape etc. are obtained from the local market in Odisha. The uniformity of surface resistivity is measured. For the plate 1 the average surface resistivity has been found to be $\sim 500k\Omega/\Box$ and that for the plate 2 has been found to be $\sim 800k\Omega/\Box$. The fabricated detector is found to be almost leak-free (it can still be improved). The testing of the module in the streamer mode for efficiency, counting rate etc. are planned for future.

6. ACKNOWLEGEMENTS

The authors thank all those who helped them in this work. We acknowledge the help by Dr. Saikat Biswas and Dr. B. Mohanty in NISER EHEP laboratory for this work.

References

[1] R. Santonico and R. Cardarelli , Nucl. Instr. and Meth. 187 (1981) 377.
[2] INO Project Report, INO/2006/01, June 2006.

.

STUDENT JOURNAL OF PHYSICS

Heat Capacity of a Quantum Dimer With General Spin S

Nick Valverde

Senior Undergraduate Student, Department of Physics and Astronomy, Arizona State University, Tempe, Arizona, USA

Abstract. In this paper we look at the thermodynamic properties of a system consisting of a quantum spin dimer for spins $S = 1/2,\ 1,\ 3/2,$ and 2 using a Hamiltonian of the form $H = -J(\vec{S_1} \cdot \vec{S_2})$ where J is the coupling constant between two spins $\vec{S_1}$ and $\vec{S_2}$. We find different and interesting behaviors in the temperature and S dependence of heat capacity depending on whether the coupling is ferromagnetic ($J > 0$) or anti-ferromagnetic ($J < 0$). Lastly, I try to shed some light on the possible causes for the observed behaviors, although some of the phenomena are not completely understood.

Keywords. Quantum dimer, Heat capacity, Heisenberg Hamiltonian.

1. INTRODUCTION

In localized magnetism one deals with single quantum spins ($\vec{S}$) interacting with each other represented by a spin Hamiltonian. Ground state and excited state properties of spin Hamiltonians have been extensively studied over the past many decades. There are quantum systems in which the basic building blocks are quantum spin clusters, QSC (dimers, trimers, tetramers etc) where the interaction between spins inside one cluster are very strong and the interaction between spins belonging to different clusters are much weaker. For these systems it is better to start with the QSC to understand their properties first and then look at the physics of interacting QSCs.

In this paper I will discuss the thermodynamic properties of a quantum spin dimers (QSD) of spin S (each member of the dimer) for S= $1/2,\ 1,\ 3/2,$ and 2. Although in most of the known QSDs the interaction between the spins is antiferromagnetic (AF), I will consider both AF and ferromagnetic cases to see how the difference in the ground state (degeneracy) and the spectral structure show up in the temperature dependence of the heat capacity C. The arrangement of the paper is as follows: first, I will discuss the model and then I will look extensively at the simplest dimer possible, which is the spin half dimer ($S = 1/2$). Following that, with some understanding of the physics of the system, I will then look at ferromagnetic and AF systems with different spin S. Lastly, several relationships arise by studying each system and discussing each behavior along with a possible reason for them.

2. THE MODEL

The system I am interested in consists of two interacting quantum spins $\vec{S_1}$ and $\vec{S_2}$ with same magnitude $S_1 = S_2 = S$. The Hamiltonian is of isotropic Heisenberg form give by

$$H = -J(\vec{S_1} \cdot \vec{S_2}). \tag{1}$$

Where J is the coupling between the two spins. The coupling constant can be thought of as how much the spins ”feel” each other. If the two spins are hardly affected by one another, then J can be taken to be small and vice versa. Both signs of J are considered, anti-ferromagnetic when $J < 0$ and ferromagnetic when $J > 0$. In order to obtain the eigenvalue of *H*, it is convenient to write *H* as

$$H = \frac{-J}{2}\Big(S_T^2 - S_1^2 - S_2^2\Big) \tag{2}$$

where $\vec{S_T}$ is the total spin operator $\vec{S_T} = \vec{S_1} + \vec{S_2}$. Since the operators S_T^2, S_1^2, S_2^2 commute with each other, they can be simultaneously diagonalized giving the eigenvalues of *H* in terms of their individual eigenvalues $S_T(S_T+1), S_1(S_1+1),$ and $S_2(S_2+1)$ respectively. For the total spin $\vec{S_T}$ there is a magnetic degeneracy where the projection of the total spin along a particular (arbitrary) direction, the $\hat{z}$-direction perhaps, $S_{T,z}$ takes the value $M = -S_T, -S_T+1, ..., +S_T$, giving a degeneracy factor $g(S_T) = 2S_T + 1$. The corresponding energy is given by

$$E(S_T) = \frac{-J}{2}\Big(S_T(S_T+1) - S_1(S_1+1) - S_2(S_2+1)\Big). \tag{3}$$

Note that these calculations can be easily generalized to the case of two dissimilar spins. Here I consider $S_1 = S_2$

Given the energy spectrum and degeneracy, it is straight forward to carry out the statistical mechanics of the system at a finite temperature T using the Canonical partition function

$$Z = \sum_{S_T} g(S_T) e^{-E(S_T)/kT} \tag{4}$$

where *k* is the Boltzmann constant. Once the partition function is found the thermodynamic identities

$$F = -kT\ln(Z)\,,\; S = -\frac{\partial F}{\partial T}\,,\; C = T\frac{\partial S}{\partial T} \tag{5}$$

can be used to find the specific heat *C* after first finding the Helmholtz free energy *F* and entropy *S*.

3. PHYSICS OF S $= 1/2$

The spin half dimer is a well documented case and can be found in many textbooks[1]. Therefore, reviewing the physics of the spin half dimer will aid in our understanding of higher spin dimer

---

[1] Schroeder, Daniel V. An Introduction to Thermal Physics. San Francisco, CA: Addison Wesley, 2000. Print.

cases. Fig. 1 gives the T dependence of the heat capacity (in units of k) obtained for a spin half dimer ($S = 1/2$). From Fig. 1 we can see that changing the nature of the coupling between the spins (equivalently, the sign of J) has a profound effect on the system. The most apparent difference is in the height of the peaks between the ferromagnetic case ($J > 0$) and the AF case ($J < 0$). The peak itself is dubbed the Schottky anomaly and the temperature this occurs at will be called T^*. This difference is due to the differences in the degeneracies of the ground and excited states between the two cases, although the total number of states are the same. For the spin half dimer, there are two configurations: the singlet ($S_T = 0$) with $g_n = 1$ and the triplet ($S_T = 1$) with $g_n = 3$. For the ferromagnetic case the ground state is the triplet, making the first excited state the singlet and the reverse situation occurs for the AF case. Thus, for positive J, when energy is added to the system the spins only have one energy state to transition to. However, in the AF case there are three options. This difference in the accessible excited states is what causes this dramatic difference in the Schottky anomaly.

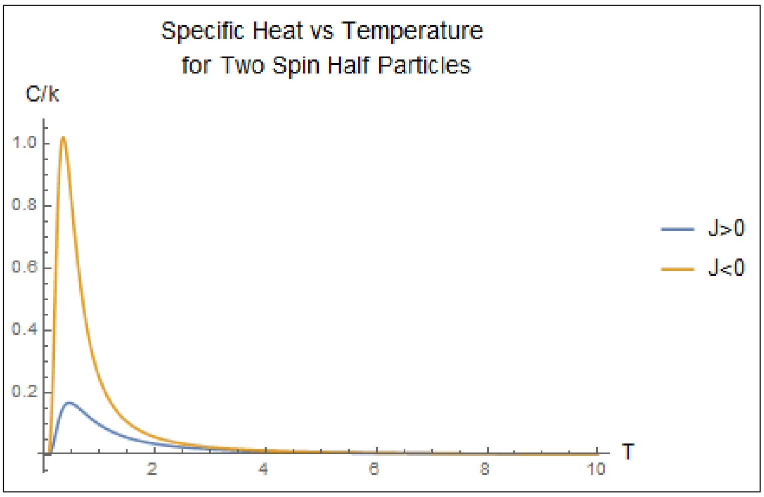

Figure 1. Heat capacity (in units of k) as a function of the temperature T for a spin 1/2 dimer for both ferromagnetic ($J > 0$) and anti-ferromagnetic ($J < 0$) coupling between the spins.

We can further understand this difference if we look at the following formula which relates specific heat to internal energy U,

$$C = \frac{\partial U}{\partial T}. \tag{6}$$

From (6), specific heat can be interpreted as the ability for a system to either absorb or release energy as the external temperature changes. Thus, the AF system is more readily able to absorb/release energy than the ferromagnetic system, which again, is due to the difference in the accessibility of excited states. Lastly, it is worthwhile to mention the low ($T << T^*$) and high temperature

($T >> T^*$) behaviors of C/k for both the cases. Looking at the figure we can discern that both cases approach zero exponentially. For the low T case, the reason is that there is not enough thermal energy for particles to make a jump to an excited state (cross gap in energy spectrum). In the high T case, there is plenty of thermal energy to allow the system to make transitions to the excited state. Each state has nearly equal probability of being occupied and thus, adding thermal energy to the system does not change the state of the system appreciably.

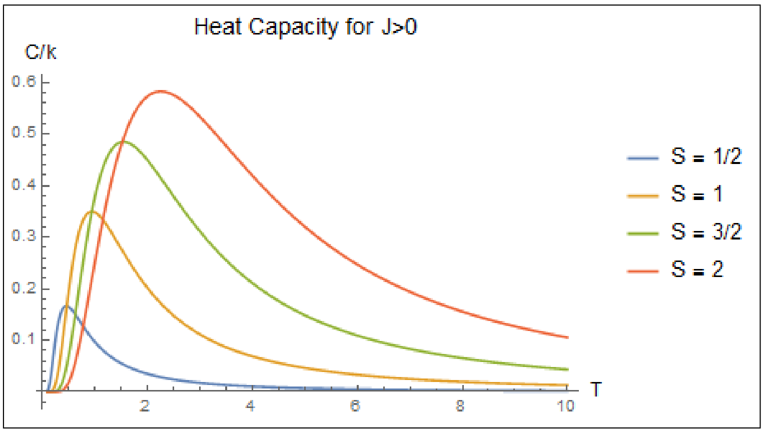

Figure 2. Heat capacity (in units of k) for ferromagnetically coupled dimers with $S = 1/2,\ 1,\ 3/2,$ and 2.

3.1 *Ferromagnetic Case* ($\mathbf{J} > \mathbf{0}$)

I will now discuss the specific heat trends for a ferromagnetic system with spin half, one, three-half, and two dimers. The specific heat curves for each case are presented in Fig. 2 where we see several interesting trends.

First, there is the increasing peak height. Looking back at equation (6) this behavior is consistent with our understanding of both the number and availability of states. As spin increases, the number of states consequently goes up. Thus, increasing spin increases the number of states the system can occupy, which makes the ability of the system to absorb energy greater. Second, peak temperature T^* of the Schottky anomaly also shifts to higher temperatures. Again, we can reason this behavior by thinking about the energy of the lowest excited states as measured from the ground state and the number of states. Since this energy difference increases with S and there are more excited states for higher spin, the system will need more thermal energy to populate these states, hence, a higher peak temperature T^*.

The ferromagnetic case presents orderly trends that make intuitive sense. Increasing the spin increases the number of states which increases the maximum heat capacity and the energy needed for C_{max} to be reached. The AF case, as we will see below, is more complex.

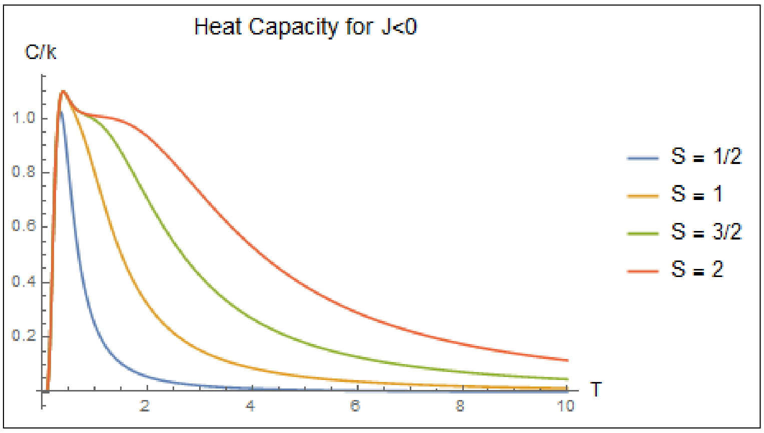

Figure 3. Heat capacity (in units of k) for AF coupled dimers with $S = 1/2,\ 1,\ 3/2,$ and 2.

3.2 *AF CASE* (**J** $<$ **0**)

Now I would like to discuss the different dimer cases for an AF system. T dependence of C/k is shown in Fig. 3.

Clearly the AF system is not as simple as the ferromagnetic system. The trends clearly presented in Fig. 2 are absent in this case. There is a particular trend that warrants further investigation. As the spin of the system is increased there is a double hump feature that begins to become more prominent. It is not until $S = 3/2$ that the double hump is clearly visible. The exact reason for this behavior is still not completely understood. But, it is speculated that this double peak feature occurs due to the competition of energy scales in the system. Thus, there is a superposition of energy spectra interfering with each other to produce the net thermal response. The energy spectrum of the AF dimer is given by Fig. 4. It is also worth noting that, again, the heat capacity for the AF system is greater than the ferromagnetic system for each corresponding S value.

4. TRENDS FOR INCREASING S

Previously, we discussed some of the trends presented in the plots of each respective dimer system. It is beneficial to make a plot of these trends and see if we can deduce the behavior as spin is increased to infinity ($S \rightarrow \infty$). The two trends examined were how the peak temperature (T^*) and the maximum heat capacity (C_{max}) change with increasing spin. Figure 5 is a graph of these trends.

Since both curves are plotted as $1/S$ moving from right to left is equivalent to starting from zero spin and proceeding to infinite spin. Fig. 5a shows how T^* varies as we increase spin. The trend

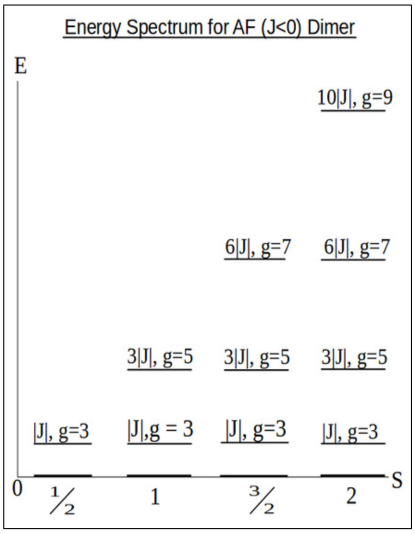

Figure 4. The energy spectrum for the AF dimer for $S = 1/2,\ 1,\ 3/2,$ and 2. Note that the ground state energies have been shifted for each dimer by a constant amount so that the ground stater energies begin at the same value $E = 0$.This constant shift does not affect the thermodynamic properties.

for the ferromagnetic system makes intuitive sense. Previously we saw this same trend for for the heat capacity curves. Increasing the spin, increases the available energy levels and, therefore, the system takes more energy to populate the states. However, the AF system has a different behavior. It increases slightly before staying constant. It is unclear why this behavior occurs and the trend is also limited, of course, by the number of data points chosen. Nonetheless I speculate that once again we are seeing some kind of competition between the number of spin configuration's degeneracy as it unfolds with increasing energy. This competition makes it difficult for the system to absorb energy based on the decreasing T^* and C_{max} values.

Fig. 5b reveals the trend for C_{max} as spin is increased. The ferromagnetic system again follows the simple intuition. The maximum heat capacity increases as we increase spin. The AF case, in addition to having an overall higher C_{max}, has a slower decrease. The decrease is subtle enough that the trend almost looks constant as in the T^* case. The physical reasoning for this behavior is not well understood and warrants further thinking to develop a deeper understanding.

5. CONCLUSION

We have seen a profound difference in the thermal response as measured through the T dependence of the heat capacity between the ferromagnetic and AF spin dimers. The trends presented for the

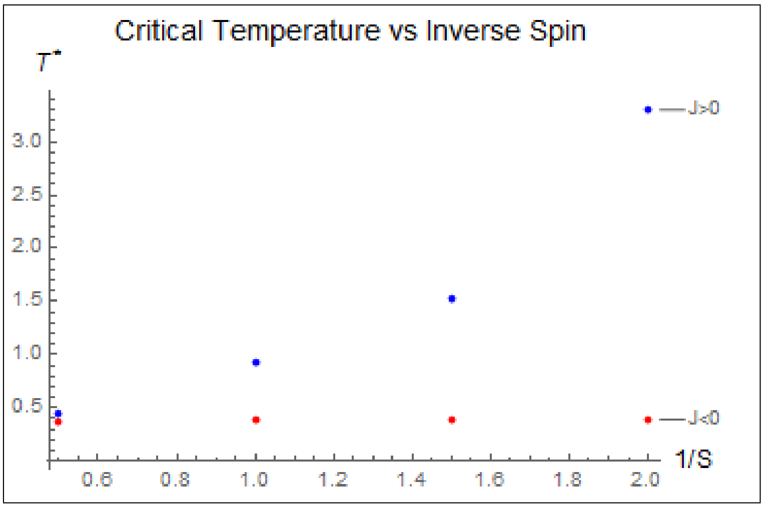

(a) T^* behavior for increasing spin.

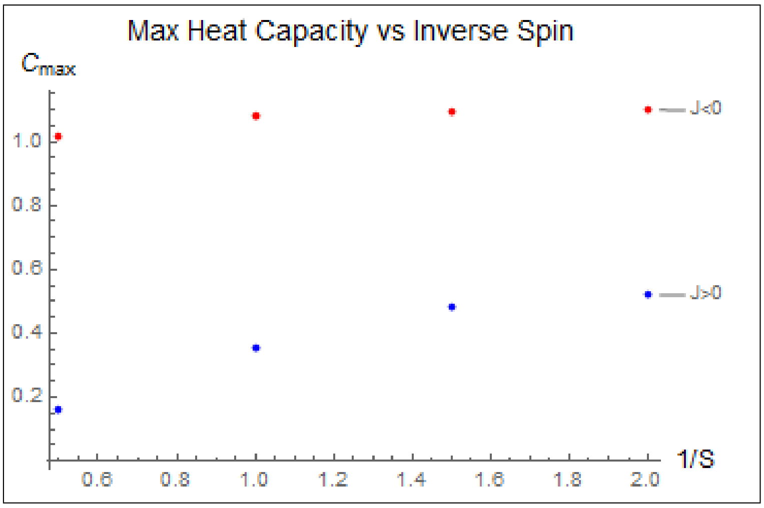

(b) C_{max} behavior for increasing spin.

Figure 5. The S-dependence of the temperature T^* at which the heat capacity is maximum, for the ferromagnetic ($J > 0$) and AF ($J < 0$) cases.

ferromagnetic case make reasonable physical sense. However, the AF system shows unusual trends consisting of the double peak structure, and the behavior T^* and C_{max} for increasing spin. It is speculated that these behaviors are due to competition of energy levels and spin configurations (degeneracies). But, it is still unknown and warrants further study.

In passing I would like to remark that as technology continues to develop magnetic systems and the underlying physics explaining them will become ever more important. For example, there is now a new field of study dealing with using spins to transmit information. Similar to the way the charge degrees of freedom of electrons are used in electronics, electronic spins will now be used in spintronics. In a magnetic system there is a plethora of interacting spins. But, one can take a simple approximation and consider a dimer in this system and use that to develop the theory further. Thus, understanding these spin configurations and their effects, is not only an intellectual curiosity but also very applicable to today's and possibly the future's technologies.

6. ACKNOWLEDGMENTS

I would like to show gratitude to Michigan State University for supporting this project during their research experience for undergraduates (REU) program.

STUDENT JOURNAL OF PHYSICS

Bound States of a Two-Dimensional Electron Gas in Inhomogeneous Magnetic Fields

Siddhant Das[*]
Elite Master Program, Theoretical and Mathematical Physics Arnold Sommerfeld Center, Ludwig-Maximilians-Universitaet, München

Abstract. We study the bound states of a two dimensional free electron gas (2DEG) subjected to a perpendicular inhomogeneous magnetic field. An analytical transfer matrix (ATM) based exact quantization formula is derived for magnetic fields that vary (arbitrarily) along one spatial direction. As illustrative examples, we consider (1) a class of symmetric power law magnetic fields confined within a strip, followed by the problem of a (2) 2DEG placed under a thin ferromagnetic film, which are hitherto unexplored. The exact Landau levels for either cases are obtained. Also, the role of the fringing magnetic field (present in the second example) on these levels is discussed.

Keywords. 2DEG, Inhomogeneous magnetic fields, Landau levels, bound states, analytical transfer matrix method

1. INTRODUCTION

The quantum mechanics of electrons constrained in two dimensions has gained a lot of interest since the advent of the (Integer) Quantum Hall and Fractional Quantum Hall Effects in the 1980s. Over the years, the experimental techniques of probing these systems with precisely structured magnetic fields at low temperatures (≈ 100 mK) have been perfected. Presently, magnetic fields that vary appreciably (even) in the nanometer scale can be created by fabricating thin films of (a) metal-excitable with a calculated current distribution, (b) ferromagnetic materials, (c) type-I superconducting materials, on a two-dimensional electron gas (2DEG) system. Interestingly, the magnetic field in these cases can be described in closed analytic form[1, 2] which, is an invitation for making very precise predictions for the behavior of 2DEGs subjected to such inhomogeneous fields. However, on the theoretical side we face a setback in considering arbitrary magnetic fields, as the Schrödinger equation describing the electron-field interaction can seldom be solved analytically, except in very simple cases. Often, powerful numerical methods offer a solution to this problem, albeit, at the loss of significant physical insight.

Considering the difficulty of a generic 2DEG-magnetic field interaction problem, we focus on a select class of magnetic fields (perpendicular to the plane of the electron gas) that are confined within an infinitely long strip of width d. Further, if the magnetic field varies across the strip (only), remaining translation invariant along the length of the strip, an exact enumeration of the bound state

---

[*] Email: siddhantdas@yahoo.co.in

energies and tunneling probabilities of the electron is possible for any form of inhomogeneity. We focus on the bound state problem here, reserving a discussion of scattering for a later paper.

Besides, a significant chunk of the literature on magnetic strips is devoted to a study of electron tunneling through the magnetic field barrier[2–5] while, relatively little is explored on the bound state solutions. Bound state solutions of a linearly varying magnetic field were obtained by Müller.[3] Even in this simple case, it is not possible to describe the electron wave functions in terms of any special function or finite analytic combinations thereof. Even otherwise, bound state solutions are exceedingly special, as their existence is not necessarily guaranteed for a given magnetic field while, scattering states always exist (for any given field variation) when the energy is above a minimum threshold value. Another nontrivial field variation that enjoys exact solvability is $\mathbf{B} = 1 - \tanh^2 x\ \mathbf{e}_z$[5] in which, the discrete and continuous part of the spectrum overlap in an energy range and are selected by the y momentum associated with the wave function.

The main goal of this paper is to find the exact bound state energies (Landau levels) for any given magnetic field variation (whenever such levels exist). We formulate the problem in Section 2 obtaining an effective one-dimensional magnetic potential for the electron. The criterion for the allowed bound state energies is obtained with an analytic transfer matrix (ATM) approach in Section 2.1. Section 3 is devoted to examples. Firstly, in Section 3.1 we obtain the Landau levels (LLs) of a magnetic strip that has a symmetric power law field variation. Following which, we consider the problem of a 2DEG placed under a ferromagnetic film in Section 3.2. Unlike in the former example, the magnetic field in this case offers a fringing field outside the strip which, has a significant effect on the LLs. We conclude in Section 4 outlining avenues of further study. An appendix at the end gives the proof of an important result used in Section 2.1.

2. PROBLEM FORMULATION

We place the 2DEG on the x–y plane, subjected to a perpendicular magnetic field

$$\mathbf{B} = B_o B(2x/d)\mathbf{e}_z, \quad \zeta \mapsto B(\zeta) \neq (=) 0, \quad |\zeta| \leq (>) 1 \tag{1}$$

where, B_o is the field strength and d is the width of the strip. $B(\zeta)$ must be integrable. The vector potential for this field, in the Landau gauge reads

$$\mathbf{A} = \frac{B_o d}{2}\Phi(2x/d)\mathbf{e}_y, \quad \Phi(\zeta) := \int_{-\infty}^{\zeta} B(\zeta')\mathrm{d}\zeta'. \tag{2}$$

We set up a minimal coupling Hamiltonian $H = (p + e\mathbf{A})^2/2m^*$ to describe the electron-field interaction where, m^* is the effective mass of the electron with charge $-e$. The magnetic length $\ell_B = \sqrt{\hbar/eB_o}$ and cyclotron frequency $\omega_c = eB_o/m^*$ provide natural length and time scales in this problem. Scaling the energy $E \mapsto (\hbar\omega_c/2)\varepsilon$ and the coordinates $(x, y) \mapsto \ell_B(\xi, \eta)$ we obtain the Schrödinger equation

$$\left\{\nabla^2_{\xi\eta} + i\frac{d}{\ell_B}\Phi\left(\frac{2\ell_B}{d}\xi\right)\partial_\eta - \left(\frac{d}{2\ell_B}\Phi\left(\frac{2\ell_B}{d}\xi\right)\right)^2\right\}\psi\left(\xi,\eta\right) = -\varepsilon\psi\left(\xi,\eta\right) \tag{3}$$

satisfied by the wave function $\psi(\xi,\eta)$. The width of the strip in ℓ_B units is given by 2β ($\beta := d/2\ell_B$). Since, the Hamiltonian has a translation symmetry in the y direction, the commutation identity $[H, p_y] = 0$ holds good. Thus, ψ is a simultaneous eigenstate of H and p_y. An ansatz $\psi(\xi,\eta) = e^{iq\eta}\varphi(\xi)$ would satisfy this requirement provided, φ solves the one-dimensional Schrödinger equation

$$\frac{\mathrm{d}^2\varphi}{\mathrm{d}\xi^2} + (\varepsilon - V_q(\xi))\,\varphi = 0, \quad V_q(\xi) := (q + \beta\Phi(\xi/\beta))^2. \tag{4}$$

We call $V_q(\xi)$ the effective magnetic potential whose, shape is modulated by the y momentum $(\hbar/\ell_B)q$ associated with the wave function. This makes the quantum mechanical behavior wave-vector dependent.[2] We will explore many interesting possibilities that arise (concerning the existence of bound states) due to the presence of q. Note that outside the magnetic strip i.e. $|\xi| > \beta$, $V_q(\xi)$ is constant as shown in Fig. 1. Specifically, for $\xi < -\beta$, $V_q(\xi) = q^2$, while for $\xi > \beta, V_q(\xi) = (q + \beta\Phi(1))^2$ where, $\Phi(1)$ is proportional to the magnetic flux per unit length linked with the infinite strip (see Equation (2)). Although, bound state solutions of equation (4) can be anticipated for energies $\varepsilon < \min\left\{q^2, (q + \beta\Phi(1))^2\right\}$; for a given $B(\zeta)$, the effective potential may not offer 'wells' for containing the electron, in which case bound state solutions will not exist for any ε. This shape dependence makes bound states rather scarce unlike scattering solutions.

2.1 *Formally exact criterion for landau levels*

In this section we use the analytic transfer matrix method (ATMM) to obtain an exact criterion for the allowed bound states in the effective potential $V_q(\xi)$. The ATMM emerged in the problem of finding guided modes of the electromagnetic field in a graded-index optical fiber.[6, 7] The method was readily extended by the pioneers to apply to one-dimensional problems in quantum mechanics[8–12] where, it has been remarkably successful not only as a calculation device for exact energy levels but also as a conceptual tool; providing deeper insights into the working and limitations of semi classical quantization schemes like the Bohr–Sommerfeld and the WKB method (and refinements of the same).[10] These efforts also led to the conceptualization of the 'modified momentum' which, substituted for the canonical momentum makes the Bohr-Sommerfeld quantization exact.[9] The ATMM, combined with super-symmetric techniques has also been applied to nontrivial potentials yielding promising results.[13]

In order to keep the paper self-contained, we give a complete derivation of the ATM quantization condition clarifying, a major ingredient in the derivation (the phase losses at the classical turning points) which, in our opinion has not been rigorously justified in previous accounts (Ref. appendix). Additionally, we evaluate the ATM quantization integral in closed form which, is a new development.

Consider two classical turning points ξ_L and ξ_R that solve $V_q(\xi) = \varepsilon$ in the region $(-\beta, \beta)$. The case of more than two turning points (as with the energy ε' in Fig. 1) is not addressed in this paper, as the ATMM is not easily generalized for multiple turning points. We partition the sub

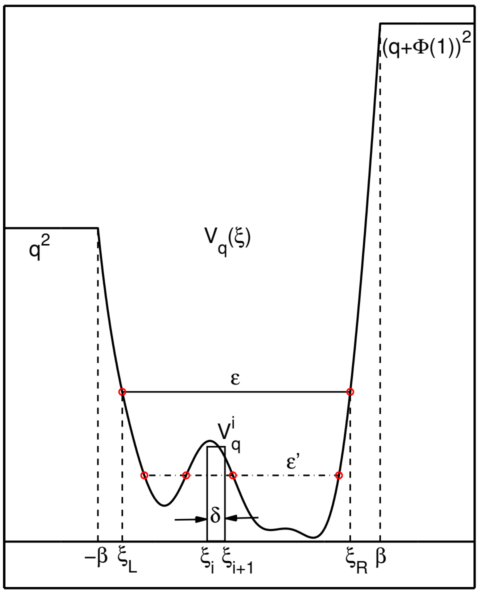

Figure 1. Sketch of the effective magnetic potential $V_q(\xi)$ with classical turning points $\xi_{L,R}$(○) for energy ε.

intervals $(-\beta, \xi_L), (\xi_L, \xi_R)$ and (ξ_R, β) into l, m and n segments respectively, each with width δ. Thus, any intermediate point $\xi_i = i\delta - \beta,\ i = 0, 1, 2 \ldots (l + m + n)$ with $\xi_{l+m+n} = \beta$. Certainly, $\xi_L = l\delta - \beta$ and $\xi_R = (l + m)\delta - \beta$. The continuous potential is now replaced by a piecewise constant equivalent over these segments, such that the potential in the segment (ξ_i, ξ_{i+1}) is $V_q^i := V_q\left(\frac{\xi_i+\xi_{i+1}}{2}\right)$. Further, the solution of equation (4) in this segment is given by

$$\varphi(\xi) = A_i e^{i\kappa_i(\xi-\xi_{i+1})} + B_i e^{-i\kappa_i(\xi-\xi_{i+1})}, \quad \kappa_i = \sqrt{\varepsilon - V_q^i} \tag{5}$$

where, $A_i(B_i)$ is the probability amplitude for the forward (backward) traveling wave component. In equation (5) φ may be tagged explicitly to show the correspondence with the i^{th} segment. We prefer to infer this from the context. Necessitating the continuity of the wave function and its derivative at the endpoints of the segment we arrive at the matrix equation

$$\begin{bmatrix} \varphi(\xi_i) \\ \dot{\varphi}(\xi_i) \end{bmatrix} = M_i \begin{bmatrix} \varphi(\xi_{i+1}) \\ \dot{\varphi}(\xi_{i+1}) \end{bmatrix}, \; M_i = \begin{bmatrix} \cos(\kappa_i\delta) & -\frac{\sin(\kappa_i\delta)}{\kappa_i} \\ \kappa_i \sin(\kappa_i\delta) & \cos(\kappa_i\delta) \end{bmatrix} \tag{6}$$

where, the overhead dot denotes differentiation w.r.t ξ. Note that $\kappa_i \neq 0$, since we assume no more than two classical turning points at this stage. Few authors prefer separate formulae for the transfer matrix M_i that hold when $\varepsilon > V_q^i$ or otherwise. In view of this distinction, our expression corresponds to the former case, while the latter case i.e. $\varepsilon < V_q^i$, leading to an imaginary κ_i is easily addressed with the analytic continuation of the trigonometric functions into the complex plane in equation (6). Thus, recovering the other expression for the transfer matrix when the case arises. With this caveat we overcome the need for selective indexing of transfer matrix products.

Left multiplying equation (6) with $\begin{bmatrix}-\dot{\varphi}(\xi_i) & \varphi(\xi_i)\end{bmatrix}$ and dividing by $\varphi(\xi_i)\varphi(\xi_{i+1})$, we obtain

$$\begin{aligned}&\begin{bmatrix}P_i & 1\end{bmatrix} M_i \begin{bmatrix}1 \\ -P_{i+1}\end{bmatrix} = 0, \qquad P_i := -\frac{\dot{\varphi}(\xi_i)}{\varphi(\xi_i)} \\ &\Rightarrow \frac{P_i}{\kappa_i} = \frac{\frac{P_{i+1}}{\kappa_i} - \tan(\kappa_i\delta)}{1 + \frac{P_{i+1}}{\kappa_i}\tan(\kappa_i\delta)}.\end{aligned} \tag{7}$$

Through the tangent addition formula we obtain

$$\begin{aligned}&\frac{P_i}{\kappa_i} = \tan\left[\tan^{-1}\left(\frac{P_{i+1}}{\kappa_i}\right) - \kappa_i\delta\right] \\ &\Rightarrow \tan^{-1}\left(\frac{P_i}{\kappa_i}\right) - \tan^{-1}\left(\frac{P_{i+1}}{\kappa_i}\right) = z_i\pi - \kappa_i\delta, \\ &z_i = 0, 1, 2, \ldots\end{aligned} \tag{8}$$

Note that $P(\xi)$ satisfies the Riccati equation

$$\dot{P} = P^2 + \varepsilon - V_q(\xi) = P^2 + \kappa^2 \tag{9}$$

which, has intimate connections with the Schrödinger equation [14]. It is often advantageous (as in the present case) to develop identities involving P. Rearranging equation (8) and summing over i from $l+1$ to $l+m$ yields

$$\begin{aligned}&\sum_{i=l+1}^{l+m} \kappa_i\delta + \sum_{i=l+1}^{l+m}\left[\tan^{-1}\left(\frac{P_{i+1}}{\kappa_{i+1}}\right) - \tan^{-1}\left(\frac{P_{i+1}}{\kappa_i}\right)\right] \\ &\quad = N\pi + \sum_{i=l+1}^{l+m}\left[\tan^{-1}\left(\frac{P_{i+1}}{\kappa_{i+1}}\right) - \tan^{-1}\left(\frac{P_i}{\kappa_i}\right)\right] \\ &\Rightarrow \sum_{i=l+1}^{l+m} \kappa_i\delta + \sum_{i=l+1}^{l+m-1}\left[\tan^{-1}\left(\frac{P_{i+1}}{\kappa_{i+1}}\right) - \tan^{-1}\left(\frac{P_{i+1}}{\kappa_i}\right)\right] \\ &\quad = N\pi + \tan^{-1}\left(\frac{P_{l+m+1}}{\kappa_{l+m}}\right) - \tan^{-1}\left(\frac{P_{l+1}}{\kappa_{l+1}}\right)\end{aligned} \tag{10}$$

The exact quantization condition emerges as a limit of equation (10) as $\delta \to 0$. In the event of $\delta \to 0$, the continuous potential variation is recovered, with $P_{l+m+1} \to P(\xi_R)$ and $P_{l+1} \to P(\xi_L)$. In the appendix we show that $P(\xi_L) < 0 < P(\xi_R)$ and $|P(\xi_{L,R})| < \infty$. Further, $\kappa_{l+1} \to \sqrt{\varepsilon - V_q(\xi_L)} = \kappa_{l+m} \to \sqrt{\varepsilon - V_q(\xi_R)} = 0$ which, gives the half phase losses at the classical turning points as

$$\lim_{\delta\to 0}\tan^{-1}\left(\frac{P_{l+m+1}}{\kappa_{l+m}}\right) = -\lim_{\delta\to 0}\tan^{-1}\left(\frac{P_{l+1}}{\kappa_{l+1}}\right) = \frac{\pi}{2}. \tag{11}$$

Further,

$$\begin{aligned}\Delta\phi_i &:= \tan^{-1}\left(\frac{P_{i+1}}{\kappa_{i+1}}\right) - \tan^{-1}\left(\frac{P_{i+1}}{\kappa_i}\right)\\ &= \tan^{-1}\left(\frac{P_{i+1}(\kappa_i-\kappa_{i+1})}{P_{i+1}^2+\kappa_i\kappa_{i+1}}\right)\\ &= -\frac{P_{i+1}(\kappa_{i+1}-\kappa_i)}{P_{i+1}^2+\kappa_i\kappa_{i+1}} + \mathcal{O}\left((\kappa_{i+1}-\kappa_i)^3\right) \qquad (12)\end{aligned}$$

which, results from expanding the inverse tangent in a tailor series in powers of $\kappa_{i+1} - \kappa_i$. Building on equation (12) we obtain

$$\lim_{\delta\to 0}\sum_{i=l+1}^{l+m-1}\Delta\phi_i = -\lim_{\delta\to 0}\sum_{i=l+1}^{l+m-1}\frac{P_{i+1}(\kappa_{i+1}-\kappa_i)}{P_{i+1}^2+\kappa_i\kappa_{i+1}}$$
$$+\lim_{\delta\to 0}\sum_{i=l+1}^{l+m-1}\mathcal{O}\left((\kappa_{i+1}-\kappa_i)^3\right) = -\int_{\xi_L}^{\xi_R}\frac{P}{P^2+\kappa^2}d\kappa = -\int_{\xi_L}^{\xi_R}\frac{P}{\dot{P}}\dot{\kappa}d\xi \qquad (13)$$

using equation (9). Thus, in the limit of $\delta \to 0$, equation (10) reads

$$\int_{\xi_L}^{\xi_R}\kappa - \frac{P}{\dot{P}}\dot{\kappa}\mathrm{d}\xi = (N+1)\pi, \quad N = 1, 2, \ldots, \qquad (14)$$

which, is an exact criteria for the bound state wave function (specified through P) and the corresponding energy that appears in P and κ. Interestingly, the above integral can be explicitly evaluated in terms of the function

$$Q := \frac{P}{\kappa} \qquad (15)$$

leading to

$$\begin{aligned}\int_{\xi_L}^{\xi_R}\frac{\mathrm{d}Q}{1+Q^2} &= \tan^{-1}\left(Q(\xi_R)\right) - \tan^{-1}\left(Q(\xi_L)\right)\\ &= (N+1)\pi, \quad N = 1, 2, \ldots,\end{aligned} \qquad (16)$$

3. EXAMPLES

3.1 *Symmetric power law fields*

A magnetic field that varies as a simple power law is obtained by choosing

$$B(\zeta) = \frac{1-|\zeta|^{\lambda-1}}{2}\left(\mathrm{sgn}(\zeta+1) - \mathrm{sgn}(\zeta-1)\right) \qquad (17)$$

We let $\lambda > 1$ to avoid a singularity at $\zeta = 0$. In the limiting event of $\lambda \to \infty$ we approach a constant magnetic field. From equation (2) we obtain

$$\Phi(\zeta) = \begin{cases} 2 - \frac{2}{\lambda}, & \zeta \geq 1 \\ \zeta + 1 - \frac{1}{\lambda}\left(1 + \mathrm{sgn}(\zeta)|\zeta|^\lambda\right), & -1 \leq \zeta < 1 \\ 0, & \zeta < -1 \end{cases} \qquad (18)$$

Substituting Φ in equation (4), we arrive at the effective magnetic potential

$$V_q(\xi) = \left(q + \xi + \beta - \lambda^{-1}\left(\frac{\mathrm{sgn}(\xi)}{\beta^{\lambda-1}}|\xi|^{\lambda} + \beta\right)\right)^2. \tag{19}$$

In this case only two classical turning points exist for any combination of parameters. Since $\Phi(\zeta)$ is an increasing curve, a well appears in $V_q(\xi)$ for $-2\beta\left(1-\frac{1}{\lambda}\right) < q < 0$ (See Fig. 2). Consequently, wave functions with $q > 0$ can only scatter through the magnetic field region.

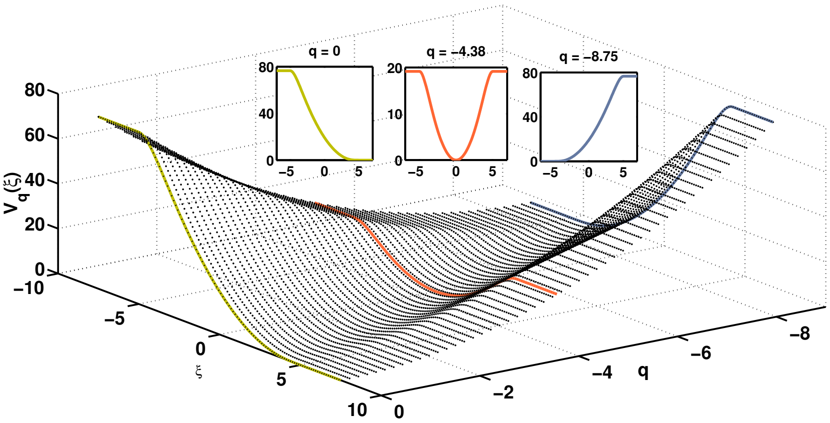

Figure 2. Surface plot of $V_q(\xi)$ for $\beta = 5$, $\lambda = 8$. In this example, wells appear when $-8.75 < q < 0$. (Insets) give the shapes of the highlighted regions where, the red curve (middle) corresponds to a symmetric well considered in equation (20).

Hence, we look for bound states in this range. Also (as noted before) the Landau levels (LLs) must populate the interval $0 < \varepsilon < \min\left\{q^2, \left(q + 2\beta\left(1-\lambda^{-1}\right)\right)^2\right\}$.

For $q = -\beta\left(1-\frac{1}{\lambda}\right)$, the well becomes symmetric about the origin, described by

$$U(\xi) := V_{\beta(1/\lambda-1)}(\xi) = \left(\xi - \frac{\mathrm{sgn}(\xi)}{\lambda\beta^{\lambda-1}}|\xi|^{\lambda}\right)^2 \quad |\xi| < \beta. \tag{20}$$

We plot this symmetric-potential-well for select values of λ in Fig. 3, with an inset displaying the variation of the well depth–given by $U(\beta) = \beta^2\left(1 - 1/\lambda\right)^2$–with λ. Note that the wells take a parabolic shape as $\lambda \to \infty$, which is the case with a constant magnetic field. Also, as $\beta \to \infty$, the effective well spans the entire axis becoming infinitely deep. Consequently, only bound states are permitted (as Landau had shown few decades ago).

From the bound state criterion derived above, we compute the first few LLs in this symmetric well in Fig. 4(a) and study their variation with λ. Clearly, the LLs asymptote to those of the limiting constant magnetic field which, are shown by means of broken lines in Fig. 4(a)—with increasing λ.

Higher levels appear progressively, since the well-depth increases with λ (Fig. 3 inset). We find that the highest LL $\sim \beta^2\,(1-1/\lambda)^2$. The well is always brim full! Combining this observation with the asymptotic behavior of the levels noted above gives an adequate estimate of the total number of LLs (say N) populating a particular well (especially as $\lambda \to \infty$).

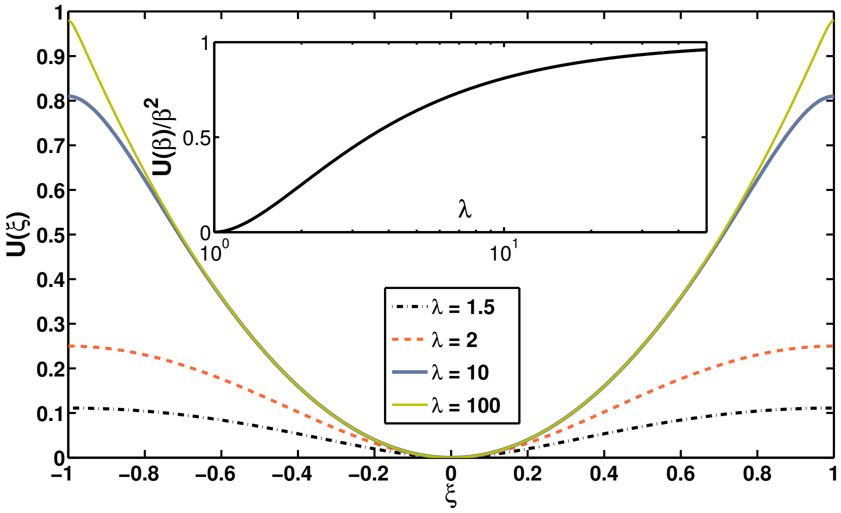

Figure 3. Plots of the effective magnetic potential $U(\xi)(=V_{(1/\lambda-1)}(\xi))$ in the region $-1<\xi<1$, $\beta=1$. (Inset) gives the asymptotic levelling of the well-depth in the event of $\lambda\to\infty$.

$$2N \sim \beta^2\left(1-\frac{1}{\lambda}\right)^2+1. \qquad (21)$$

In Fig.4(b) we superpose the LLS of the previous case with those corresponding to a larger $\beta=10$. Numerous higher levels (red dots) appear due to the increase in the well-depth. Further, with increasing λ, the LLs for either values of β almost overlap which is emphasized by the boxed region in Fig.4(b).

Note that, even in the limit of $\lambda\to\infty$ (describing a constant magnetic field) the width of the strip remains finite (since β is fixed); quite insensitive to which, the LLs asymptote to the LLs of a spatially-unbounded uniform field (the Landau Problem). We recall that in the former case the wave functions outside the strip decay exponentially (since the effective potential is constant out side the strip) while, those in the latter case have Gaussian tails. It thus turns out, despite a finite width, the LLs overwhelmingly approach those of the spatially-unbounded uniform magnetic field for large enough values of λ.

3.2 *2DEG under a ferromagnetic film*

The symmetric power law magnetic fields considered above cannot be realized with the experimental methods discussed in Section 1. However, they serve as good approximations to realistic magnetic fields. A crucial element that lacks in these ideal geometries is the presence of a fringing field outside the strip. For large sample sizes the fringing field can often be neglected. In this spirit, we had required that the magnetic field be strictly zero outside the strip (equation (1)). Consequently, $V_q(\xi)$ became constant for $|\xi| > \beta$, and an exact criterion for the LLs could be obtained.

Now, we relax this constraint and allow the field to out-flank the strip; with an understanding that the field vanishes progressively with distance from the strip. For these fields, most of the treatment remains same as before, except for a truncation of the effective potential far away from the classical turning points, which turns out to be a valid approximation, if the LL under consideration is much below the height of the effective potential at the truncation points.[11, 12] The consequent error can be overcome by choosing truncation points sufficiently far from the turning points, allowing the LLs of interest to settle within the desired precision.

Consider a 2DEG placed under a ferromagnetic film at a distance z below it. For a vertically magnetized film of width (thickness) $d(a)$ and magnetization per unit width σ, the magnetic field on the 2DEG is given by (see Fig.5)

$$\begin{aligned}
&\mathbf{B}(x,z) = B_o B(\zeta)\mathbf{e}_z, \\
&B(\zeta) = 2\left\{\frac{(\zeta+1)}{(\zeta+1)^2+z_o^2} - \frac{(\zeta-1)}{(\zeta-1)^2+z_o^2}\right\}, \\
&B_o := 2a\sigma,\ z_o = 2\frac{z}{d}
\end{aligned} \tag{22}$$

when, $a/d, a/z \ll 1$.[2] The length of the strip is infinite as before. Using equation (2) we obtain

$$\Phi(\zeta) = \ln\left(\frac{(\zeta+1)^2+z_o^2}{(\zeta-1)^2+z_o^2}\right) \tag{23}$$

which, leads to the effective magnetic potential

$$V_q(\xi) = \left\{q + \beta\ln\left(\frac{(\xi+\beta)^2+\theta^2}{(\xi-\beta)^2+\theta^2}\right)\right\}^2 \tag{24}$$

In obtaining the effective potential we scaled $z = \ell_B\theta$ and used the definition $z_o = 2z/d = (2l_B/d)\theta = \theta/\beta$.

Due to the interplay of the parameters describing the effective-potential, many interesting possibilities arise. First of all, unlike in the former example, $V_q(\xi)$ varies (appreciably) over the entire ξ axis tending to q^2 as $|\xi| \to \infty$. Secondly, the effective potential in this case possesses a special reflection symmetry $V_{-q}(\xi) = V_q(-\xi)$, which implies that the energy eigenvalues of equation (4) for bound state solutions remain invariant under the transformation $q \mapsto -q$. Thus, the LLs are *doubly* degenerate. From this property, it suffices to study the spectrum for $q > 0$. Further, for an

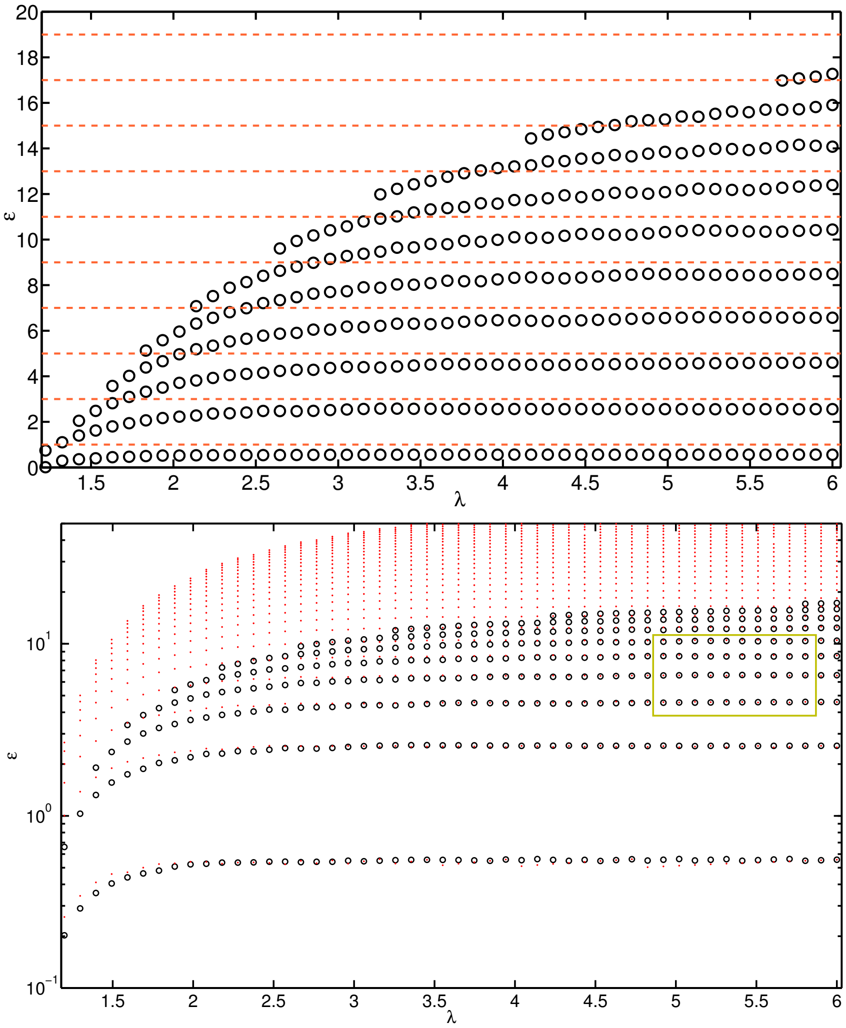

Figure 4. Plot of first few LLs (black circles) corresponding to different λ for $\beta = 5$. Horizontal broken lines give the LLs for a uniform, infinitely extending magnetic field ($LL_{l+1} = 2l + 1, l = 0, 1, 2 \ldots$). Black circles in the figure at bottom are same as those in the figure at top, while red dots give the LLs for $\beta = 10$.

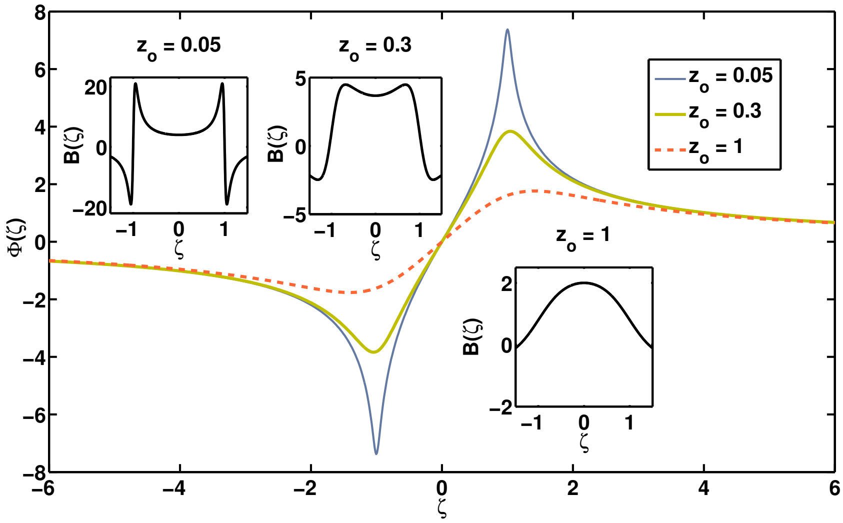

Figure 5. Plot of $\Phi(\zeta)$ vs. ζ for $z_o = 0.05,\ 0.3,\ 1$. (Insets) show the magnetic field variation $B(\zeta)$ for these values of z_o.

energy ε, there can exist at the most four classical turning points given by

$$\xi = -\beta\coth\phi_\pm \pm \left(\beta^2\text{csch}^2\phi_\pm - \theta^2\right)^{\frac{1}{2}} \quad \phi_\pm = \frac{q \pm \sqrt{\varepsilon}}{2\beta} \tag{25}$$

one or more of which might vanish–in the event of $\phi_+, \phi_- = \ln\left(\beta/\theta \pm \sqrt{1+(\beta/\theta)^2}\right)$–get repeated or become complex. In the interest of bound states, four (distinct) turning points may correspond to an energy within a double-well shaped potential, while two repeated (coincident) turning points would occur when the energy hits the top of the barrier between the two wells. And, higher energies would give rise to (only) two real turning points. These cases are illustrated in Fig. 6(a). A clearer perspective of the 'motion' of the tuning points (in the complex ξ plane) is obtained by examining their loci (Ref. Fig. 6(b)) parameterized by the energy.

Next, we discuss the LLs supported by the effective potential. At the present moment the correct generalization of the ATMM criterion for more than two classical turning points is not clear, which prevents us from obtaining the LLs (lying below the barrier top) for the double well shown in Fig. 6(a). However, the interested reader is referred to the work of L. V. Chebotarev on the 'Extensions of the Bohr–Sommerfeld formula to double- well potentials'[15] which, can be used to find the (approximate) LLs for this case.

In the event of $\theta > \beta,\ q > 2\beta\tanh^{-1}(\beta/\theta)$ the effective potential (in this case) offers a single well (Ref. Fig.7(a)) with two classical turning points at $\xi = -\beta\coth\phi_- \pm \left(\beta^2\text{csch}^2\phi_- - \theta^2\right)^{1/2}$. The LLs in this case can be computed with our ATM quantization criterion. Using equation (4) we obtain the LLs for this single well which, are plotted in Fig.7(b) for various values of q. Note that as q increases, the minimum value (bottom) of the effective potential $\min(V_q)$, also increases, hence

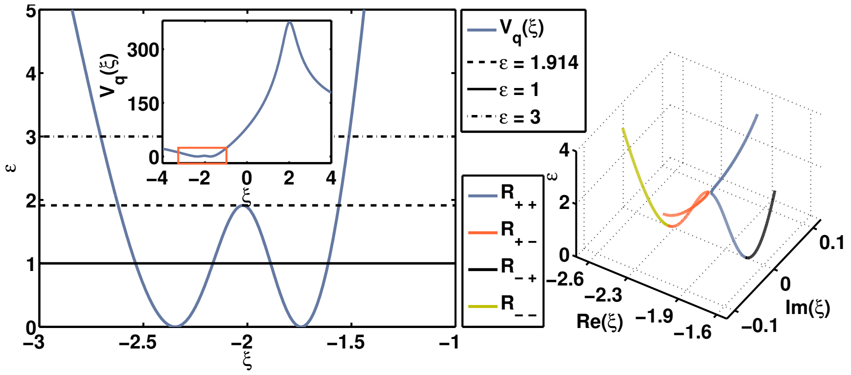

Figure 6. (a) Plot of $V_q(\xi)$ vs. ξ for $\beta = 2,\ \theta = 0.3,\ q = 9$ showing a double-well potential. Horizontal energy lines intersect the potential at the (real) classical turning points. (Inset) displays the same potential on a larger range of ξ. (b) Loci of the classical turning points $R_{ab} = -\beta \coth \phi_a + b \left(\beta^2 \mathrm{csch}^2 \phi_a - \theta^2\right)^{1/2}$, $ab = \pm$ (Ref. equation (24)) parameterized by ε taken along an axis perpendicular to the complex ξ plane.

the lowest Landau levels increase in energy. In fact, the well depth, i.e. $q^2 - \min(V_q)$ also increases with q, unfolding higher LLs. However, the rate of emergence of new LLs becomes slower with increasing q as shown in Fig.7(b) inset.

Before concluding, we discuss the effect of the fringing magnetic field pervading the region outside the strip, i.e. $|\xi| > \beta$. Generally, with increasing distance from the ferromagnetic film, i.e. $\theta \gg \beta$ the fringing field can be neglected. However, the fringing field itself gave rise to many interesting effective potential shapes (unlike in the previous example). Particularly, in the preceding single well case with $\theta = 2\beta$, we find that the effective well manifests in the interval $-5\beta < \xi < 0$, which lies outside the strip. This also gives a clue as to where the probability density of the electron is likely to be accumulated.

4. CONCLUSION

In this paper we considered the problem of finding the bound state solutions of an infinite 2DEG subjected to a perpendicular magnetic field that varies (arbitrarily) in one direction only. An exact criterion for the bound state energies or Landau levels was developed using the analytic transfer matrix method (ATMM) for the case when the effective magnetic potential allowed two (real) classical turning points. The extensions of the ATMM for more than two turning points is not clear at the present moment and calls for further consideration. Applying our formalism to a symmetric power law magnetic field led to the exact LLs, whose variation with the strip-width β and field exponent λ were studied. In the sequel we looked at a 2DEG placed under a ferromagnetic film, which is an experimentally realizable system. Fortunately, this example could be tracked analytically to a great

a. Effective magnetic potential $V_q(\xi)$ for $\beta = 2$, $\theta = 4$, $q = 3$ with 13 LLs depicted by horizontal lines.

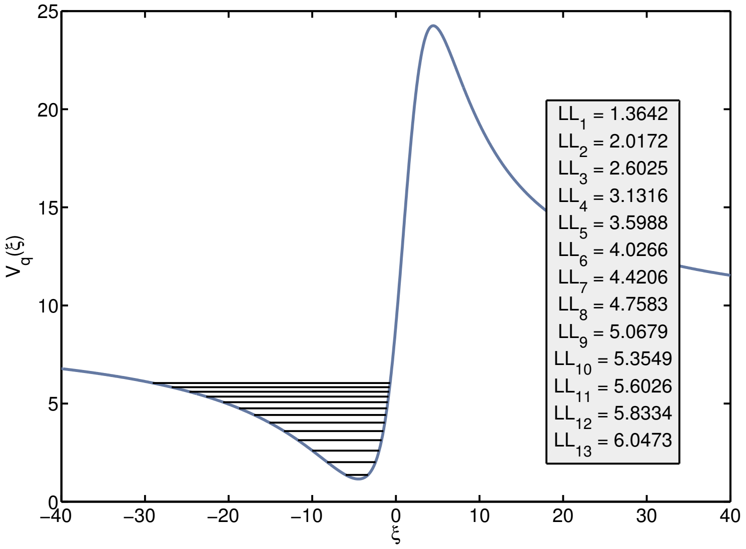

b. Plot of allowed LLs with $\beta = 2$, $\theta = 4$ and $q > 2\beta \tanh^{-1}(\beta/\theta) \sim 2.197$. (Inset) Plot of # of LLs and the well depth $= q^2 - \min(V_q)$ vs. q.

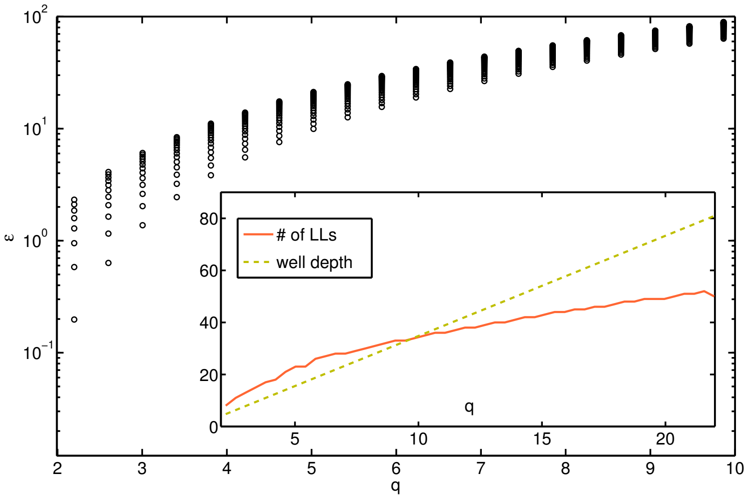

Figure 7.

extent and the LLs for a single (effective) well were obtained for various values of the y-momentum $(\hbar/\ell_B)q$. This example also emphasized the role of the fringing field on the Landau levels.

5. ACKNOWLEDGEMENTS:

I gratefully acknowledge the help of Prof. Dr. Hemalatha Thiagarajan whose, meticulous proofreading drew my attention to many errors which, I believe have been corrected. I also benefited from the discussions with Dr. Sumiran Pujari on the ATM quantization formula.

Appendix.

Let $\psi(x)$ be a bound state solution of the one-dimensional Schrödinger equation

$$\frac{\mathrm{d}^2\psi}{\mathrm{d}x^2} + (E - V(x))\psi = 0. \tag{A.1}$$

Based on the properties of an admissible bound state wave function we deduce an important property of the auxiliary function

$$P(x) = -\psi^{-1}\frac{\mathrm{d}\psi}{\mathrm{d}x} \tag{A.2}$$

which, is well defined (and bounded) at any finite x excepting the nodes of the wave function. We show that

$$P(x) < (>)0, \qquad x = x_L\,(x_R) \tag{A.3}$$

at the left (right) *most* classical turning point $x_L(x_R)$ that solves $V(x) = E$. Using this result we obtain the half phase loss at the turning point $x_R(x_L)$ to be $+\,(-)\,\frac{\pi}{2}$. It is implicit that we are working with a real ψ, hence the inequality in proposition (A.3) is valid.

Proof: The points where $V(x) < (>)E$ constitute the classically allowed (forbidden) region. Consider the following properties

1. $|\psi| \to 0, |\psi'| \to 0$ as $|x| \to \infty$
2. $\psi \neq 0$ for any x (no nodes) in the classically forbidden region

which, hold good for any bound state wave function. Since, equation (1) is form invariant under the transformation $x \mapsto -x (\Rightarrow x_L \mapsto x_R)$ while $\mathrm{d}/\mathrm{d}(-x) \mapsto -\mathrm{d}/\mathrm{d}(-x)$, it suffices to prove any one of the two propositions in (A.3). We focus on the left most classical turning point x_L. The truth of proposition (A.3) at this point rejects the possibility $\mathrm{sgn}\,[\psi(x_L)] = -\mathrm{sgn}\,[\psi'(x_L)]$; sgn[ ] being the signum function. To prove this we let $\psi(x_L) > 0 > \psi'(x_L)$. From property 2, it follows that $\psi(x) > 0$ for all $x < x_L$ (a classically forbidden region). Therefore, $\psi'' > 0$ (from equation (A.1)–(A.2)). Since, ψ is increasing (away from the origin) at x_L, it must attain at least one maxima before it asymptotes to the real axis (as $x \to -\infty$) remaining positive-definite all along. Clearly, at the site of this maximum $\psi^{''} < 0$ which is not possible. The other possibility $\psi(x_L) < 0 < \psi'(x_L)$ (a 'reflection' of the previous case) is readily contradicted from form-invariance of equations (A.1)–(A.2) under the transformation $\psi \mapsto -\psi$.

Finally, we show that

$$|P(x_{L,R})| < \infty \tag{A.4}$$

Proof: Since, ψ and ψ' cannot vanish simultaneously, [16] we need only show that a classical turning point cannot be a node of the wave function. Consider x_L as before. Assume $\psi'(x_L) \neq \psi(x_L) = 0$. From property 1, $\psi \to 0$ as $x \to -\infty$. Thus, ψ must admit at least one minima (maxima) if $\psi'(x_L) < 0(> 0)$ remaining negative (positive) definite all along. However, this contradicts the fact that $-\infty < x < x_L$ is classically forbidden.

References

[1] A. Nogaret, Electron dynamics in inhomogeneous magnetic fields. Journal of Physics: Condensed Matter, 22(25), 253201 (2010).

[2] A. Matulis, F. M. Peeters, & P. Vasilopoulos, Wave-vector-dependent tunneling through magnetic barriers. Physical Review Letters, 72(10), 1518 (1994).

[3] J. E. Müller, Effect of a nonuniform magnetic field on a two-dimensional electron gas in the ballistic regime. Physical Review Letters, 68(3), 385 (1992).

[4] Y. Guo, H. Wang, B. L. Gu, & Y. Kawazoe, Electric-field effects on electronic tunneling transport in magnetic barrier structures. Physical Review B, 61(3), 1728 (2000).

[5] M. Calvo, Exactly soluble two-dimensional electron gas in a magnetic-field barrier. Physical Review B, 48(4), 2365 (1993).

[6] Z. Cao, Y. Jiang, Q. Shen, X. Dou, & Y. Chen, Exact analytical method for planar optical waveguides with arbitrary index profile. JOSA A, 16(9), 2209–2212 (1999).

[7] Z. Cao, Q. Liu, Y. Jiang, Q. Shen, X. Dou, & Y. Ozaki, Phase shift at a turning point in a planar optical waveguide. JOSA A, 18(9), 2161–2163 (2001).

[8] Z. Cao, Q. Liu, Q. Shen, X. Dou, Y. Chen, & Y. Ozaki, Quantization scheme for arbitrary one-dimensional potential wells. Physical Review A, 63(5), 054103 (2001).

[9] Z. Liang, Z. Q. Cao, X. X. Deng, & Q. S. Shen, Generalized quantization condition, 22(10), 2465–2468 (2005).

[10] Z. Cao, & C. Yin, Advances in One-Dimensional Wave Mechanics. Springer (2014).

[11] A. Hutem, & C. Sricheewin, Ground-state energy eigenvalue calculation of the quantum mechanical well $V(x) = 1/2kx^2 + \lambda x^4$ via analytical transfer matrix method. European Journal of Physics, 29(3), 577 (2008).

[12] H. Ying, Z. Fan-Ming, Y. Yan-Fang, & L. Chun-Fang, Energy eigenvalues from an analytical transfer matrix method. Chinese Physics B, 19(4), 040306 (2010).

[13] H. Sun, The Morse potential eigenenergy by the analytical transfer matrix method. Physics Letters A, 338(3), 309–314 (2005).

[14] S. B. Haley, An underrated entanglement: Riccati and Schrödinger equations. American Journal of Physics, 65(3), 237–243 (1997).

[15] L. V. Chebotarev, Extensions of the Bohr–Sommerfeld formula to double-well potentials. American Journal of Physics, 66(12), 1086–1095 (1998).

[16] For a bound state wave function ψ, if $\psi(x) = \psi'(x) = 0$ at any finite x (with $|V(x)| < \infty$), then ψ must vanish identically.

STUDENT JOURNAL OF PHYSICS

Classification of Variable Stars Based on their Photometric Colours

Jinsu Ann Mathew[‡,*], **Sheelu Abraham**[‡,†], **Ninan Sajeeth Philip**[†‡]
[‡] Final Year, M.Sc., Santhom Computing Facility, St. Thomas College, Kozhencherry -689641, Kerala, India
[†] Santhom Computing Facility, St. Thomas College, Kozhencherry -689641, Kerala, India

Abstract. We present photometric classification of variable stars (transients) based on their colours using General Catalogue of Variable Stars (GCVS) that has the coordinates of about 47,000 variable stars in addition to the information on their type, period of variability etc. The magnitude of a subset of these objects were obtained from Sloan Digital Sky Survey (SDSS) Data Release 10 (DR10). The colour distribution of different variable stars in various colour space were studied using TOPCAT. We conclude that colour can be used with reasonable confidence to guess the nature of the transient.

Keywords. Variable stars, Photometric colours.

1. INTRODUCTION

Stars emit radiation in almost all wavelengths in the electromagnetic spectrum. Their mass varies from a fraction of the solar mass to 10 - 100 solar masses. The colour of the star depends on their temperature. The hottest star emits blue light and has a temperature of $50,0000^0\ C$. A star of lesser temperature would be bluish-white in colour, followed by white, yellowish-white, yellow, yellow-orange, orange-red. The coolest of the visible stars would be deep red. Since stars emit outside the visible spectrum of the electromagnetic radiations, a more precise definition of colour is used in astronomy context.

Astronomers usually subdivide the entire electromagnetic spectrum into different bands of frequency (wavelengths) and represent the flux in each band on a logarithmic scale known as magnitude. Since this flux may vary in different bands for the same object, depending on how its spectra looks like, the magnitude is defined for each band. Thus the flux emitted by a star in the wavelengths close to green colour may be called g-band magnitude or simply g-magnitude. But since the visible region is a very narrow band, we also have infrared bands like i-magnitude, K-magnitude etc. Now colour need not mean the same blue, green colours and in the astronomical context it is defined as the difference in the magnitude between two different bands of the electromagnetic spectra.

Almost all stars vary their brightness as a function of time. Variable stars are those that vary brightness beyond a certain threshold from their mean magnitudes. Some of these variable stars exhibit periodic behaviour, while some others exhibit a once-off dramatic change in brightness by

---

[*] jinsuann91@gmail.com
[†] sheelu@iucaa.com
[‡] nspp@iucaa.ernet.in

several orders of magnitude before fading away. These changes may take place within a day, a week, a month, a year, or over many years. There are a number of reasons for variability. These include changes in star luminosity, star mass, obstructions in the amount of light that reaches earth etc. Since the cause of light variation is different, variable stars are classified into different groups.

Variable stars are mainly classified into intrinsic and extrinsic variables. In the case of an intrinsic variable star, the variation is due to the physical changes in the star or stellar system. This type of stars provides a large amount of information about the internal structure of the star that helps astronomers to model the stellar evolution. Pulsating stars and eruptive or cataclysmic variable stars belong to this category. Extrinsic variable stars are those in which the light output changes due to some process external to the star itself. That is, variation is caused by the eclipse of one star by another or by the effect of stellar rotation. The two main classes of extrinsic stars are the eclipsing binaries and rotating variables. Variable stars are usually studied utilising the light curve data. In this study, we make use of photometric colour information to classify variable stars.

2. MATERIALS AND METHODS

The main objective of this paper is to identify features other than light curve data for the classification of the variable stars. The methodology is to use variable stars with known type and see how well they are separated in the colour space. Since colour is one of the easiest features that can be obtained, it will greatly aid automated classifications if they can produce moderate segregation between the different classes. The Virtual Observatory platform developed by astronomers offers several good tools to do these things and some of them that we used for this study are briefly described below.

Vizier

Vizier catalogue service [1] is an astronomical catalogue service provided by Centre de donnes astronomiques de Strasbourg. It provides access to the most complete library of published astronomical catalogues and data tables available online. These catalogues are arranged in a self-documented database.

General Catalogue of Variable Stars

The General Catalogue Of Variable Stars [GCVS; 2] is a reliable reference source on all known variable stars. The catalogue contains 47,969 variable stars and information regarding their positions, variable type and period.

Sloan Digital Sky Survey

The magnitudes of the objects were obtained from the Sloan Digital Sky Survey [SDSS, 3]. SDSS is one of the most influential surveys in astronomy through which multicolour images covering more than a quarter of the sky were obtained to create a 3-dimensional map containing more than 9,30,000 galaxies and more than 1,20,000 quasars. SDSS has five filters u, g, r, i and z so it is possible to obtain 10 different colours.

TOPCAT

Tool for operations on catalogues and tables [4] is an interactive graphical viewer and editor for tabular data. It provides many facilities for the analysis and manipulation of source catalogues and other tables. TOPCAT provides fast access to large data, performs flexible or fast matching of rows in the same or different tables, concatenate the rows of existing tables to create new ones, allow different plots, broadcast tables with other VO tools etc.

DATA

As mentioned earlier, the data for this study is obtained from GCVS. Out of the 47,969 variable stars in GCVS, only 7453 comes in the sky covered by (footprint of) SDSS. Out of this, 3679 are pulsating, 1168 are eclipsing, 930 are eruptive, 377 are rotating and 163 are cataclysmic. Each of this class is subdivided into many subclasses according to their mass, period etc. To make sure that the plots have enough points, we took 12 of these classes that had at least fifty points in each. The number and type of stars selected from each class are described below.

Pulsating

Twenty two different classes of objects were present in this main group and from this we obtained six. We have used the same notations as given in the GCVS catalogue for representing the variable stars. They are:

LB: Slow irregular variables of late spectral types, usually giants. 561 LB type stars were available.

M: Mira type variables. These are long-period variable giants with characteristics emission spectra. They have longer periods which lie in the range between 80 and 1000 days. 446 M variables were available.

RRAB: RR Lyrae variables with asymmetric light curves. The period ranges from 0.3 to 1.2 days, and amplitudes from 0.5 to 2 magnitude. 1302 RRAB were available in our data sample. RRC: RR Lyrae variables with nearly symmetric, sometimes sinusoidal, light curves. Period ranges from 0.2 to 0.5 days and amplitude is less than 0.8 magnitude. 233 RRC variable stars were available.

SR: Semiregular variables, which are giants or supergiants of intermediate and late spectral types showing noticeable periodicity in their light changes, accompanied by various irregularities. 248 SR variable stars were present in the sample.

SRB: Semiregular giants with poorly defined periodicity (means cycles in the range of 20 to 2300 days). Sometimes the simultaneous presence of two or more periods of light variation is observed. Our data sample contains 261 SRB variable stars.

Eruptive/cataclysmic

By the same criteria described before, we shortlisted three type of variable stars out of 15 classes in this group. They are:

UVN: Red dwarf stars showing outbursts up to 6 magnitudes lasting for only a few minutes caused by flares. There are 312 UVN stars available in our sample.
INB: Orion variables, young stars and protostar in or near nebulae. These stars produce irregular variations up to several magnitudes. 235 such variables are present in the sample.
UG: Close binary systems consisting of a dwarf or subgiant star. Orbital periods are in the range 0.05 to 0.5 days. These system acts as source of x-ray emission. 66 UGs were available.
Eclipsing Out of five eclipsing star types, only two had enough representation in our sample.
EA: Algol type eclipsing system. An extremely wide range of period is observed from 0.2 to ¿= 10000 days. 346 EAs were present in our sample.
EW: Eclipsing systems with period shorter than 1 day. The depth of primary and secondary minima are almost equal or differ insignificantly in EW variables. 486 EWs were available in the data.

Rotating
Among the three type of rotating stars only BY type had sufficient sample size.
BY: Emission line dwarfs showing quasi-periodic light changes with periods from a fraction of a day to 120 days. There exist 290 BYs in the sample.

Thus, a total of 4786 variable stars were used in the present study.

3. RESULTS AND CONCLUSION

From the five magnitudes of SDSS, we obtained ten colours. The colours used are $u-g$, $g-r$, $r-i$, $i-z$, $u-r$, $g-i$, $r-z$, $u-i$, $g-z$ and $u-z$. Out of this, $u-g$, $g-r$, $r-i$, $i-z$ are called primary colours. Plot window of topcat allows us to draw two dimensional scatter plots of one or more pairs of table columns and three sample cases are shown below.

As seen, the BY type stars were concentrated around grids 1 to 3 of $u-g$ and -2 to 2 of $r-z$ while UG type concentrated mainly around grid 0 of both $u-g$ and $r-z$.

Similarly, EA is located from 0 to 2 of $u-g$ and around 0 of $g-z$. SRB stars were concentrated between 2 to 4 of $u-g$ and 0 to 5 of $g-z$.

Analysis of the graph shows that the UG stars are centered on grid 0 of $u-r$ and are positioned in between -1 and 1 on $r-z$. RRAB stars are placed from grids, -2 to 2 on $u-r$ and mainly from -1 to 3 on $r-z$.

Verification of classification accuracy using CRTS variable star data

Now that we have observed significant separation between the different classes of stars, we extended our study to classify the variable stars detected by the Catalina Real-Time Transient Survey [CRTS; 5,6]. CRTS is a synoptic sky survey started with the goal to explore and characterize the faint variable sky. It is the first sky survey which publishes all optical transients immediately after detection through various electronic mechanisms such as Skyalert [7] and CRTS home page.

Figure 4 displays the distribution of cataclysmic variables, considered for the study, in SDSS

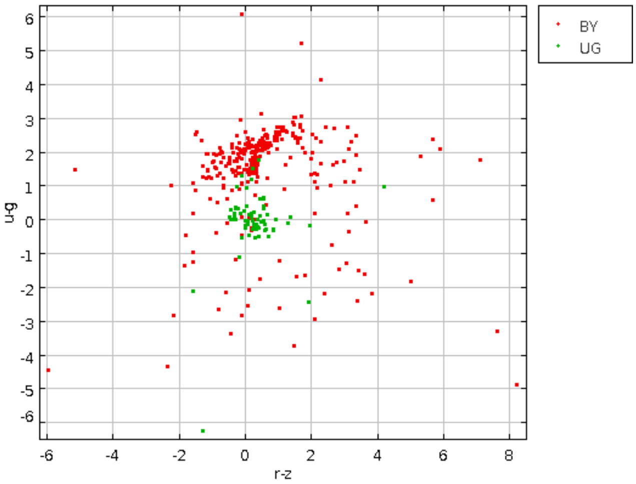

Figure 1. Colour space diagram of rotating type (BY) and eruptive type (UG) in $u - g$, $r - z$ colour space.

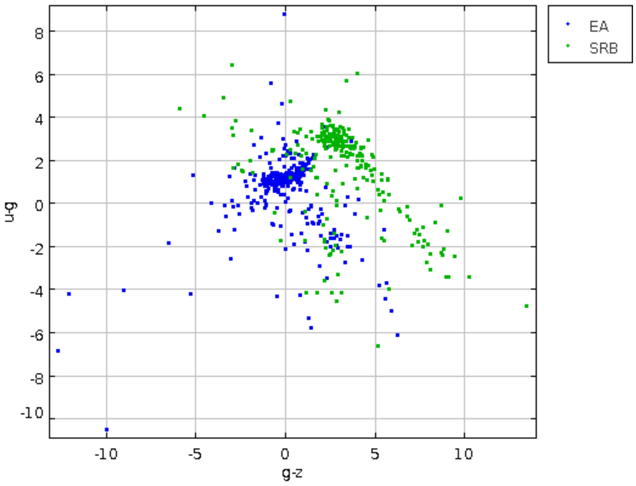

Figure 2. Colour space diagram of Algol type eclipsing (EA)and Semi Regular type(SRB) in $u - g$, $g - z$, colour space.

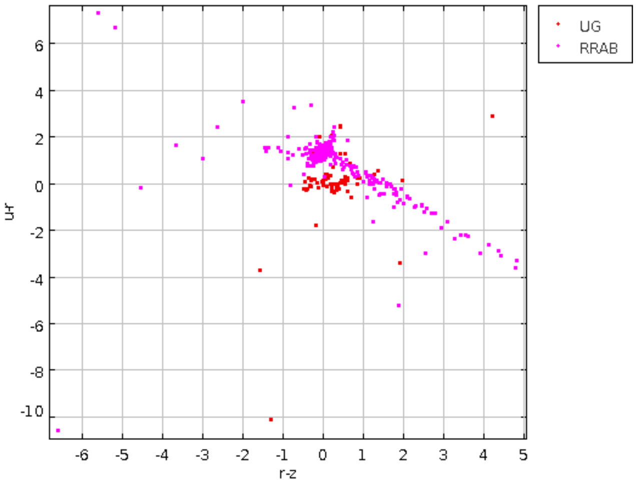

Figure 3. Colour space diagram of eruptive type (UG) and RR Lyrae type (RRAB) in $u - r$, $r - z$ colour space.

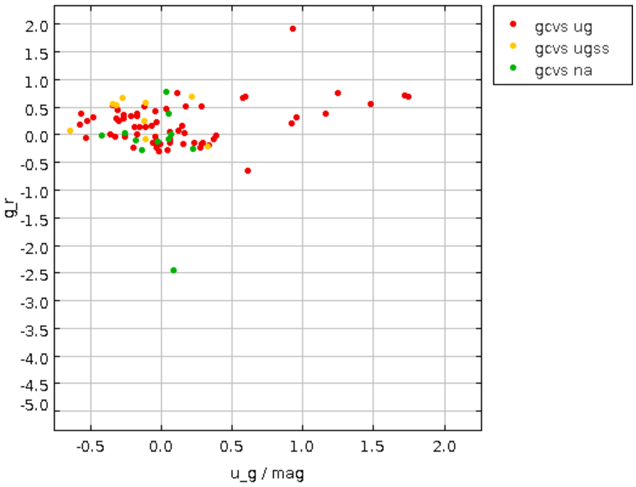

Figure 4. Colour distribution of cataclysmic variable star in GCVS catalogue.

$g - r$, $u - g$ colour space. The main subclasses considered in cataclysmic variable star are UG, UGSS and NA.

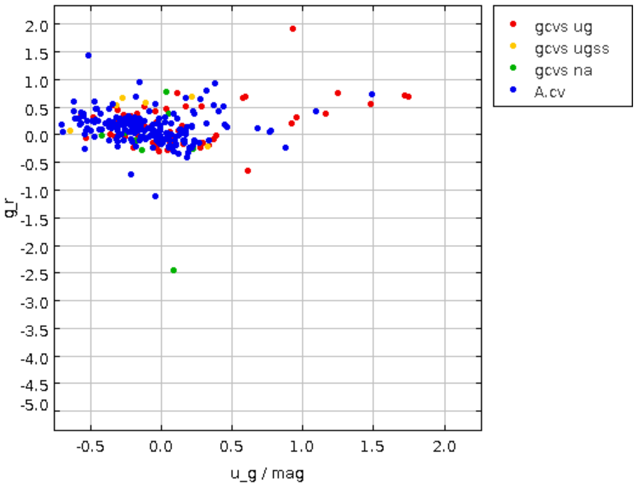

Figure 5. Colour distribution of cataclysmic variables in GCVS and CRTS. The blue points represents the cv in CRTS while others are from GCVS. The figure is obtained by overplotting cataclysmic variables of CRTS with GCVS data shown in figure 4. The cataclysmic variables in CRTS lie in the same region of colour feature space where the GCVS variables are.

4. CONCLUSION

In this work, colour distribution of different variable stars in the same colour space was plotted using TOPCAT. The results show that various types of stars can be easily identified in colour space.

References

[1] Ochsenbein, F., Bauer, P., and Marcout, J. 2000, Astronomy and Astrophysics Supplement, 143, 23.

[2] Samus, N. N., Durlevich, O. V., et al. 2009, VizieR Online Data Catalog, 1.

[3] York, D. G., et al. 2000, AJ, 120, 1579.

[4] Taylor, M. B. 2005, Astronomical Data Analysis Software and Systems XIV, 347, 29.

[5] Djorgovski, S. G., Drake, A. J., and Mahabal, A. A., et al. 2011, arXiv:1102.5004.

[6] Drake, A. J., Djorgovski, S. G., and Mahabal, A., et al. 2012, IAU Symposium, 285, 306.

[7] Williams, R. D., Djorgovski, S. G., Drake, A. J., Graham, M. J., and Mahabal, A. 2009, Astronomical Data Analysis Software and Systems XVIII, 411, 115.

.

Study of Interdiffusion of Calcium Chloride-Water system Using Laser Beam Deflection Sensor

T.M. Sreedevi[1], **N.P. Dhanya**[2], **P.R. Sasikumar**[3]
[1] M Sc (Physics, Fourth Semester) SNM College, Maliankara.
[2] IKKTM. Govt. College, Pullut.
[3] Maharajas College, Ernakulam -682011, Kerala, India

Abstract. Deflection of a laser beam on passing through an interdiffusing transparent medium of calcium chloride-water system is monitored and explained. A fanned out laser beam using a cylindrical lens is found to follow a Gaussian profile corresponding to the refractive index gradient in the inter diffusing medium. The emerged deflected beam profile at different time depends on the diffusion coefficient. Square of the full width at half maximum of this Gaussian concentration gradient profile is directly proportional to the diffusion coefficient. Exponential decrease of diffusion rate with time is also reported. The diffusion coefficient of calcium chloride in water at room temperature is calculated with better accuracy, and this study can be extended to study diffusion of many transparent, completely miscible samples in micro and nano scales.

Keywords. Laser beam deflection sensor, diffusion.

1. INTRODUCTION

Diffusion, which is the movement of solute particles from higher concentration to lower concentration plays a vital role in many fields like physics, biochemistry, pharmacology, low gravity experiments, food synthesis, etc. The slow rate of diffusion is responsible for its importance because in many cases it limits the overall rate of the transport process. For example, the electrical properties of semiconductor devices are controlled by diffusion of charge carriers, rate of chemical reaction in chemical processes depends on the diffusion of anions and cations, in biological systems the food intake, action of drugs and medicines etc. depends on diffusion phenomena. Diffusion often limits the efficiency of commercial distillations and the rate of industrial reactions using porous catalysts. It limits the speed with which acid and base react and the speed at which the human intestine absorbs nutrients. It controls the growth of micro organisms, the rate of corrosion of steel, and the release of flavour from food. Ficks law of diffusion uses a diffusion coefficient for the description of diffusion phenomena [1].

When two transparent miscible liquids with different solute concentrations are allowed to mix slowly, a refractive index gradient (RIG) is formed at the interface due to the concentration gradient from which an incident laser beam can be deflected (LBD) and studied [2-6]. The deflection suffered by the beam is a direct measure of the diffusion parameters inside the liquid. Being an optical sensor, LBD provides an accurate result. In this study diffusion of calcium chloride solution at known concentration in water is discussed.

2. EXPERIMENTAL SETUP AND MEASUREMENTS

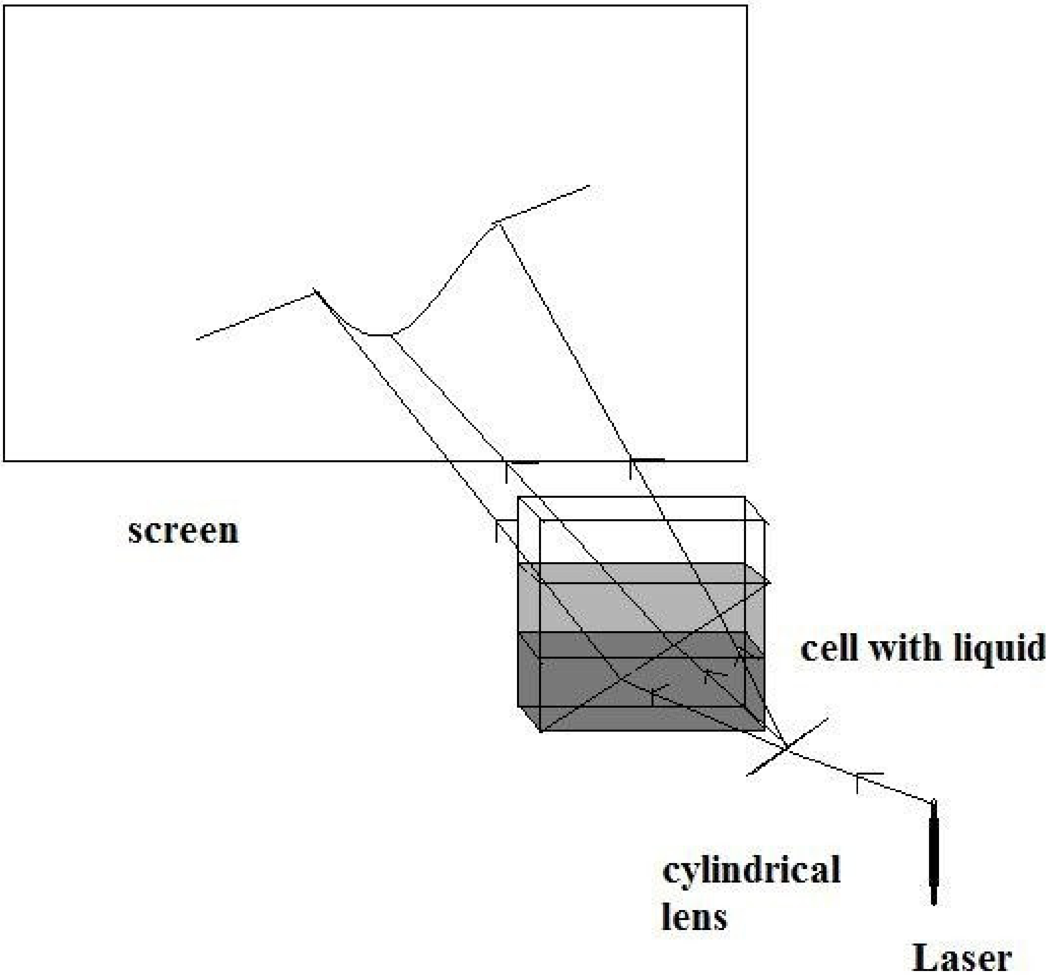

Figure 1. The experimental set up for Laser beam deflection measurement.

The dimension of the experimental cell is $6 \times 4.5 \times 2 cm^3$ with $1.2 mm$ thick glass plates on both sides of a stainless steel body. The screen is arranged at $1.5 m$ from the cell. A fanned out laser beam is created by passing it through a cylindrical lens mounted at 45^o with the vertical. The emergent beam is allowed to fall diagonally on a cuvette containing the liquid where there is a concentration gradient of calcium chloride (Fig.1). Calcium chloride solution with specific molarity is prepared by taking 20 ml of water in the cell and the prepared solution is pipetted to the bottom of the cell avoiding random mixing so that a sharp boundary between the liquids is formed with low concentration solution above and high concentration solution below the boundary. After some initial turbulence the deflection of the beam by the RIG is traced out on the screen at different time intervals till the mixing almost completes. The observed LBD pattern is shown in Fig. 2.

Figure 2. The Laser beam deflection pattern seen in the experimental setup of Fig.1.

3. MATHEMATICAL EQUATIONS

Taking a step like variation of concentration in a plane with in the medium, we can write [3,5]

$$\frac{\partial C}{\partial y} = \frac{C}{2\sqrt{\pi X t}} \exp\left(\frac{-y^2}{4Dt}\right) \tag{1}$$

This is a Gaussian function and will be of the same shape traced out by the deflected beam at the boundary.

The shape of beam trajectory inside the liquid is given by a Gaussian function.

$$Z(y) = k \exp\left(\frac{-y^2}{4Dt}\right) \tag{2}$$

Here $Z(y)$ is the deflection of the laser beam on the screen, y is the depth of deflecting region within the cell below the interface, k is a proportionality constant. As time evolves the boundary smears out until the concentration gradient disappears. This results in the broadening of the Gaussian function. We can evaluate the diffusion constant D from the half width ($y_{1/2}$) of the Gaussian function as

$$D = \frac{y_{1/2}^2}{4tln2} \tag{3}$$

4. RESULTS AND DISCUSSIONS

The image of the deflected beam is traced out on the graph paper for analysis. The observations are made for various time intervals for the same concentration and each time D is calculated. A graph is plotted between dC/dy and y (Fig. 3). The FWHM ($y_{1/2}$) of the graph is measured for a particular time interval. This is repeated for different time intervals. A graph is plotted between $(y_{1/2})^2$ and time interval and its slope is used to evaluate D (Fig. 4). The measured value of diffusion coefficient of calcium chloride in water is $6.9505 \times 10^{-5} cm^2/sec$ which is in close agreement with the reported value [7]. As the diffusion progresses, the depth of the beam deflection decreases and

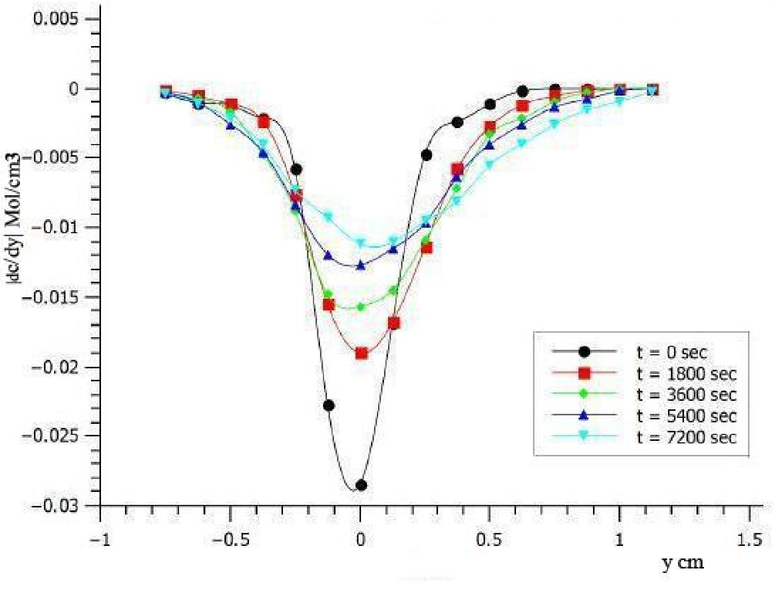

Figure 3. Plot of concentration gradient against deflection at different times.

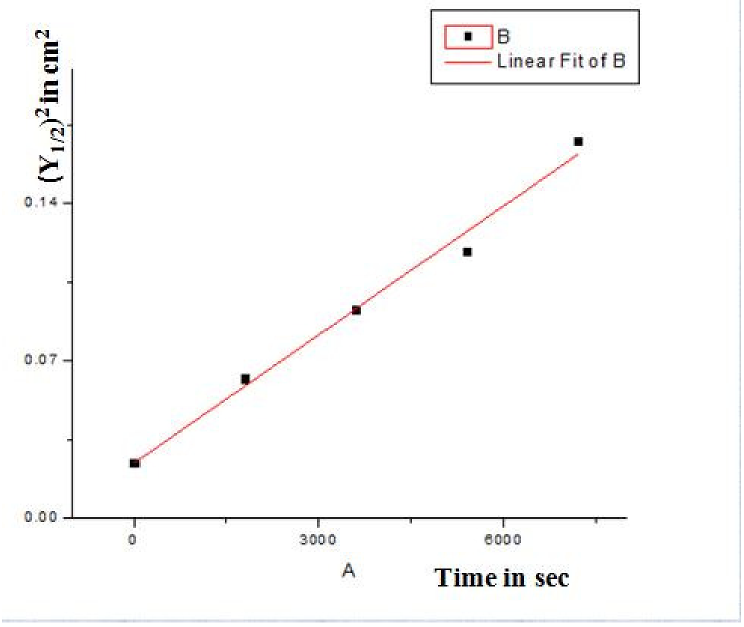

Figure 4. Square of FWHM $(y_{1/2})^2$ vs. time graph.

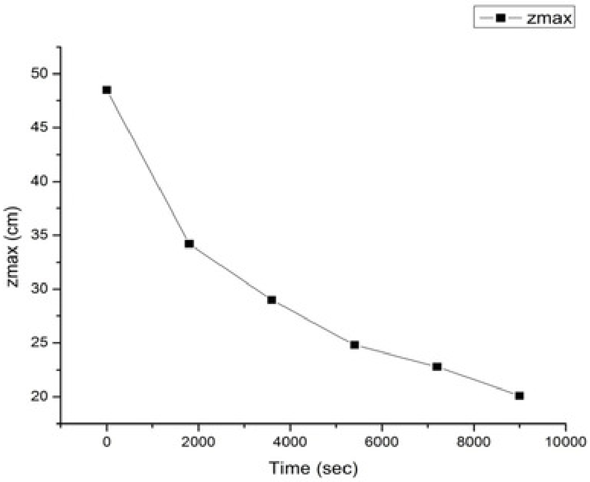

Figure 5. Variation of maximum deflection Z_{max} with time.

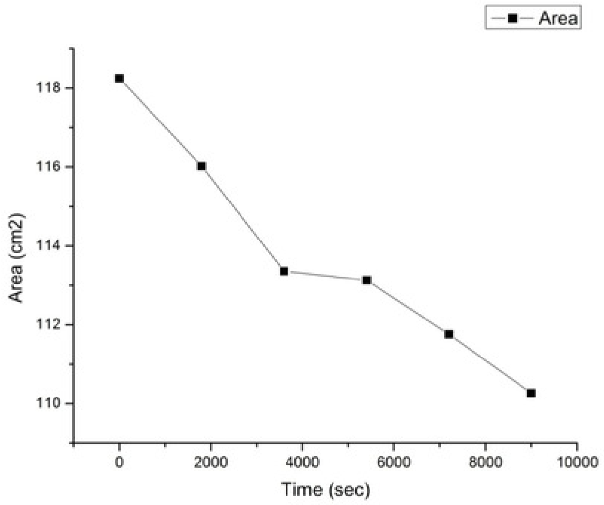

Figure 6. Variation on the area of deflection pattern with time.

the pattern broadens with time (Fig. 3). This is a clear indication of the dependence of refractive index gradient in the liquid medium on time. Plot of maximum deflection, Z_{max} with time (Fig. 5) indicates that diffusion is fast in the beginning and decreases almost exponentially with time. Area of the laser beam deflection pattern also decreases linearly with time.(Fig. 6)

The experiment is repeated several times and the results obtained are in close agreement with the standard values of D obtained by various methods[3-5].

5. CONCLUSION

Diffusion study of calcium chloride in water using LBD sensor is demonstrated. The amplitude of the deflection which is proportional to the concentration gradient is found to decrease exponentially with time.

ACKNOWLEDGMENT

NPD is grateful to Directorate of Collegiate Education, Trivandrum and Mahatma Gandhi University, Kottayam for supports.

References

[1] Cussler E.L., Models for Diffusion in Diffusion Mass Transfer in Fluid Systems,3rd Ed. New York: Cambridge University Press,2009 pp1-pp3.

[2] Arun Anand, Vani K Channiwal, and C.S. Narayanamurthy (2015, Jan.) ”Diffussivity study of transparent liquid solutions by imaging beam deflection”, Researchgate [online] pp 1-7 www.researchgate.net.

[3] Achamma Kurien *et. al.*, ”Application of laser beam deflection technique to study the diffusion process in electrolyte solutions”, Pramana-J of Phy, Vol. 43, No.5, pp401-406, Nov.1994.

[4] Andreas MANDELIS, Ryoychi TAKAUE, Zhuohui CHEN, Joanna SZURMAK, and W. Douglas BAINES, ”Quantitative Laser Beam deflection study of Liquid-Liquid inter diffusion in the water-sugar system”, Analytical Sciences, Vol.8, pp131-136, Apr. 1992.

[5] Dhanya N.P. and P.R. Sasikumar,(2014 Aug), ”Measurement of diffusion coefficient of glucose in water by laser beam deflection method” presented at Current trends in Material Science, pp 100-105.

[6] F. Francini, P.K. Buah Bassuah, and F.T. Arecchi , ”Scanning beam technique to measure small diffusion coefficients” Optic communications, Vol.105, No.5-6, pp285-288, Feb.1994.

[7] ”Handbook of Chemistry and Physics Education”, CRC Press, New York (2003) 74th edition.

.

A Numerical Eploration of the Parameter Plane in the Prey - Predator Model

P. K. Thankam[†], P. P. Saratchandran[‡] and K. P. Harikrishnan[‡][*]
[†] M. Sc. Student, Department of Physics, The Cochin College, Cochin-682 002, India.
[‡] Department of Physics, The Cochin College, Cochin - 682002, India.

Abstract. We undertake a detailed numerical investigation of the parameter plane of the discrete prey-predator model with the natural death rate of predator in the absence of prey equal to zero. We identify the various dynamical regimes in the parameter plane numerically. Our numerical studies reveal the presence of a region where the asymptotic state deviates from the analytically expected value. We attribute this to the competition between the prey and the predator for survival. We also undertake a dimensional analysis to compute exactly the border line seperating the the periodic and chaotic domains in the parameter plane.

Keywords. Prey-predator Model, Bifurcations, Chaos

1. INTRODUCTION

The problem of the competition between populations of two species is an old one and different models have been proposed to understand its mechanism. The first model in this regard was proposed by the mathematician Voltera [1] in the form of a system of differential equations:

$$\begin{aligned} \frac{dx}{dt} &= ax(1-x) - bxy \\ \frac{dy}{dt} &= -cy + dxy \end{aligned} \tag{1}$$

where $x(t)$ and $y(t)$ represent the population density of prey and predator at time t and a, b, c and d are positive parameters. Here a represents the natural growth rate of the prey in the absence of predators and c represents the natural death rate of predator in the absence of prey. The terms $(-bxy)$ and $(+dxy)$ describe the prey-predator encounters which are favourable to predators and fatal to prey. The dynamics of the prey-predator system has been studied by many authors [2–4].

Note that the above model cannot show any chaotic behavior as it is a two dimensional flow. In fact, discrete models are more reasonable to describe the interaction between species as discussed in detail by May [5]. Such models are more efficient for numerical studies as well and exhibit much richer dynamical structures including chaos, compared to continuous time models. Several such prey-predator and host-parasite models have been formulated and analysed in the past [6–8]. Here we consider the discrete version of the basic prey-predator model corresponding to Eq.(1). There are two versions for this model, one with the natural death rate of predator in the absence of prey $c \neq 0$

---

[*] email : $kp\_hk2002@yahoo.co.in$

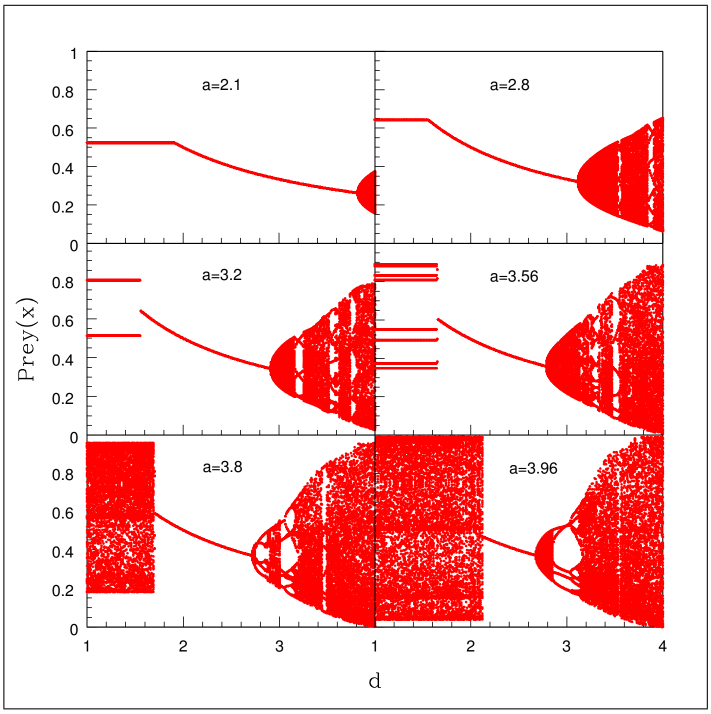

Figure 1. The bifurcation structure of the prey-predator model showing how the population of prey (x) changes with d as the control parameter, for six different values of a. Three different phases can be clearly seen in all cases. The first part indicates period doubling bifurcations to chaos as a varies from 1 to 4 (logistic dynamics), with predator population $y_n \to 0$ for small d. The second phase is a stable fixed point for both x and y which decreases in size as a increases. The last phase represents the post Hopf bifurcation with limit cycles and periodic windows on the way to chaos as d increases. Chaos appears only for sufficiently large values of (a, d).

and the other with $c = 0$. The first version has been studied analytically and numerically by Jing and Yang [9] and Elsadany et al. [10]. The second version with $c = 0$ has been studied in detail by Danca et al. [11] and showed the presence of stable periodic regions, bifurcations and chaos in the model. We undertake a detailed numerical analysis of the complete parameter plane of this model. We identify the exact region of chaos in the parameter plane. Moreover, we show numerically the existence of a small region in the parameter plane where the competition between the predator and prey forces the predator into extinction, beyond the region of extinction obtained analytically. We also undertake a dimensional analysis of the chaotic attractors of the model.

The paper is organised as follows: The next section presents a stability analysis of the model to identify the stable one cycle region. Our main results are discussed in Section 3, where a detailed numerical analysis of the model is undertaken. Conclusions are drawn in Section 4.

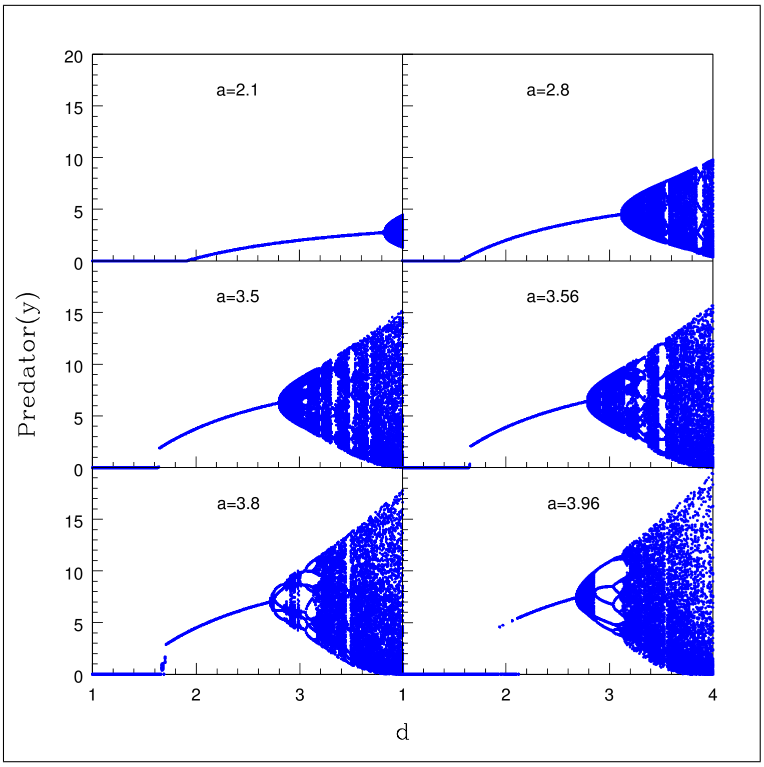

Figure 2. Same as the previous figure, but for predator population y instead of x. Again, three phases can be seen for all a values with the first phase corresponding to predator extinction with $y_n \to 0$. Note that this phase first decreases with a and then increases (that is, extends to larger range of d values) as a becomes large.

2. STABILITY ANALYSIS AND PERIODIC REGIME

The discrete model we consider is given by

$$\begin{aligned} x_{n+1} &= ax_n(1-x_n) - bx_ny_n \\ y_{n+1} &= dx_ny_n \end{aligned} \tag{2}$$

There are two stable fixed points of the map given by

$$(x_1^*, y_1^*) = (0,0), (x_2^*, y_2^*) = (\frac{1}{d}, \frac{a}{b}(1-\frac{1}{d}) - \frac{1}{b})$$

Taking the linearised Jacobian matrix J, the stability of a fixed point can be established by calculating the eigen values λ of J corresponding to the fixed point using the characteristic equation

$$|J - \lambda I| = 0$$

For (x_1^*, y_1^*), we get $\lambda_1 = 0, \lambda_2 = a$. Thus $(0,0)$ is stable if $a < 1$, irrespective of the value of b and d and both prey and predator vanish asymptotically.

For the second fixed point, $y_2^* > 0$ for $d > \frac{a}{a-1}$. Moreover, the eigen values $\lambda_{1,2}$ corresponding to (x_2^*, y_2^*) are

$$\lambda_{1,2} = (1 - \frac{a}{2d}) \pm \frac{1}{2}\sqrt{(\frac{a}{d}+2)^2 - 4a} \tag{3}$$

The condition $\lambda_{1,2} < 1$ is satisfied for $d > \frac{a}{a-1}$ and $a > 1$. Thus the condition

$$d = \frac{a}{a-1} \tag{4}$$

represents a curve in the parameter plane $a - d$ below which the dynamics of prey is governed by the logistic map with a as the control parameter with the population of predator $y_n \to 0$.

Above this curve, the fixed point (x_2^*, y_2^*) becomes stable and one expects a stable one cycle for the co-existence of prey and predator. The region of stability for the fixed point (x_2^*, y_2^*) can be determined by looking at the characteristic equation for J at the fixed point, which can be shown to be

$$P(\lambda) = \lambda^2 - Tr\lambda + Det = 0 \tag{5}$$

where Tr is the trace and Det is the determinant of the Jacobian matrix $J(x_2^*, y_2^*)$ and are given by

$$Tr = 2 - \frac{a}{d} \tag{6}$$

$$Det = a(1 - \frac{2}{d}) \tag{7}$$

If the eigen values λ_i for $J(x_2^*, y_2^*)$ are inside the unit circle in the complex plane, then the fixed point (x_2^*, y_2^*) is locally stable. The necessary and sufficient condition for this are given by

i. $P(1) = 1 - Tr + Det > 0$
ii. $P(-1) = 1 + Tr + Det > 0$
iii. $P(0) = Det < 1$

By substituting the values of Tr and Det, the above 3 conditions can be shown to be equivalent to

$$d > \frac{a}{a-1} \tag{8}$$

$$d > \frac{3a}{a+3} \tag{9}$$

$$d > \frac{2a}{a-1} \tag{10}$$

Thus, the region of stability for the fixed point (x_2^*, y_2^*) is determined by the condition

$$d \in (\frac{a}{a-1}, \frac{2a}{a-1}) \tag{11}$$

The fixed point becomes unstable through a Hopf bifurcation producing a limt cycle. Thus the line of Hopf bifurcation in the parameter plane is given by the condition

$$d = \frac{2a}{a-1} \tag{12}$$

Above this line, the asymptotic state is a limit cycle which may be periodic or quasi periodic depending on the values of a and d. As a and d increases further, the system shows more complex behavior including chaos. We now explore this region of the parameter plane numerically in detail to identify the chaotic regime.

3. NUMERICAL RESULTS

From the analytic results obtained in the previous section, it becomes clear that the value of the parameter b cannot control the asymptotic dynamics; it only determines the position of the attractor in the phase plane. Hence we fix the value of b as 0.2 in all the computations. Since the growth rate of prey in the absence of the predator is governed by the logistic dynamics, we restrict the value of a and d to a maximum of 4. Also, for $a, d < 1$, both x_n and $y_n \rightarrow 0$. Hence effectively, the parameter plane $(a - d)$ is restricted within the range $[1 - 4]$. For $a > 4$, the trajectory escapes to ∞. In all our numerical simulations, we use the initial condition x_0, y_0 as $0.63, 0.18$. But we have checked that the results remain unchanged for any initial value in the unit interval $[0, 1]$.

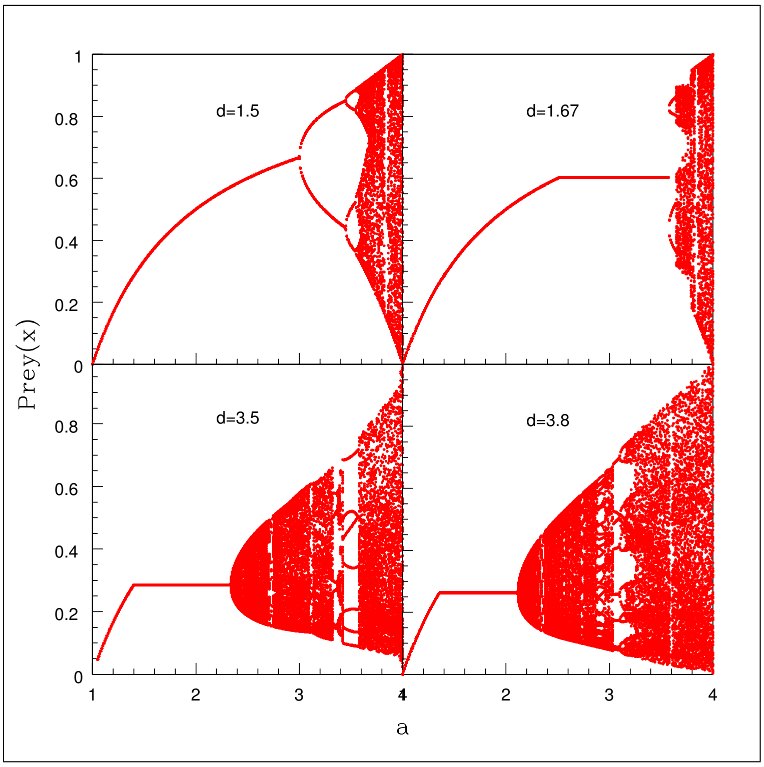

Figure 3. The bifurcation structure for prey population with a as the control parameter for different fixed values of d. When d is sufficiently low (say,$d = 1.5$), the bifurcation structure is clearly that of the logistic map. As d increases, 3 phases can be seen as in Fig. 1 with stable one cycle, Hopf bifurcation and finally chaos. For a small range of d values, (example $d = 1.67$), the dynamics once again re-enters the extinction phase for predator with x values fluctuating with logistic chaos.

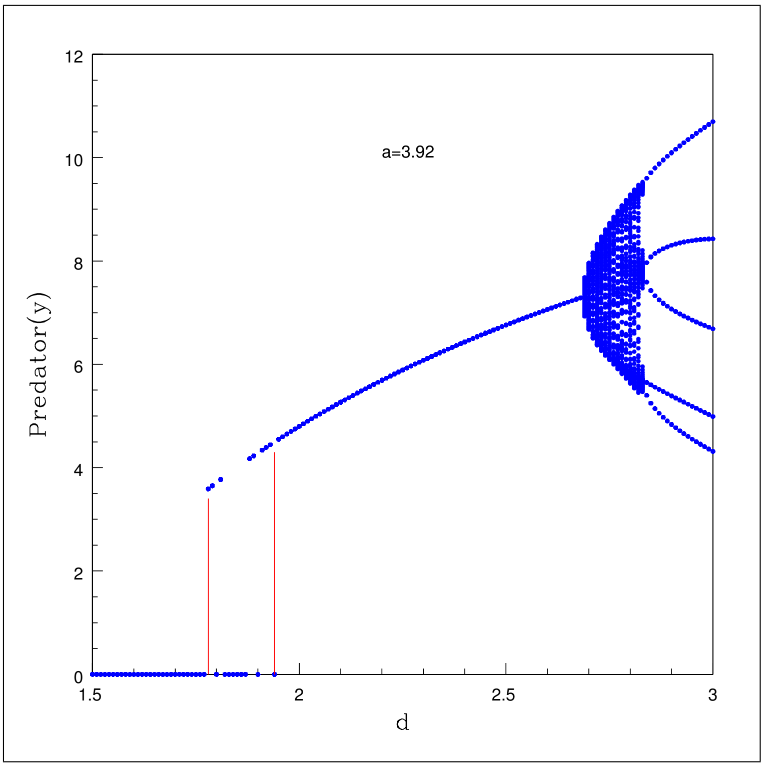

Figure 4. A part of the bifurcation structure for predator with d as the control parameter. There is a small region shown within the two vertical lines where the dynamics sensitively depends on the value of d. The asymptotic state may switch between 0 and a stable state for an infinitesimal change in the control parameter d.

We first compute the bifurcation structure of the prey-predator model for the population of the prey (x) and pedator (y) seperately as a function of d for several fixed values of a in the range $[1, 4]$. The results are shown in Fig. 1 and Fig. 2 respectively for six different values of a. Three seperate phases can be clearly seen in both the figures. The first phase (for small d) indicates period doubling bifurcations to chaos for prey as a increases from 1 to 4. which is just the logistic dynamics in the absence of the predator, $y_n \to 0$. The second phase corresponds to stable co-existence of prey and predator, and its range steadily deceases with a. As the parameter is further increased, the system undergoes a Hopf bifurcation producing a limit cycle (third phase) and finally becomes chaotic at values of a and d as discussed in detail below. Note also that the range of the first phase decreases with a initially, but extends to larger values of d as a increases. This result is completely unexpected, since analytically the domain of predator extinction decreases continuously with a as per Eq.(5). We explore this numerical result in more detail below.

In Fig. 3, we show the bifurcation structure for prey population with a as the control parameter for different fixed values of d. As expected, when d is small, the bifurcation structure is that of the logistic map. When d is sufficiently large, three phases can be clearly seen, namely, predator extinction, stable one cycle and domain of Hopf bifurcation and chaos. For a small range of intermediate d values (for example, $d = 1.67$), the dynamics re-enters the extinction phase for predator where analytically one expects a stable phase. It is clear that there is a small region in the parameter plane where the competition between the predator and prey becomes critical in determining the asymptotic state of the combined system. As the growth rate of prey dominates, the population of the predator is quenched into extinction, stretching the domain of extinction well into the stable region.

Another interesting result we have obtaiined numerically is the identification of a very small regime on the border between the domain of extinction and the stable domain where two stable asymptotic states become riddled depending on the parameter value. In other words, the asymptotic state is sensitively dependent on the parameter value and can switch between two stable states with an infinitesimal perturbation to the parameter. The predator population can switch between stability and extinction while the population of the prey can correspondingly switch between stability and chaotic oscillation. This can be seen from Fig. 4 which is a part of the bifurcation structure for predator with d as the control parameter. There is a small region shown within two vertical lines where the asymptotic state switches between zero and a stable state for an infinitesimal change in the control parameter d. A magnified view of this region is shown in Fig. 5 to make this more clear, along with the corresponding asymptotic state for prey.

As the parameter values are increased, the fixed point becomes unstable through a Hopf bifurcation producing a limit cycle. This is shown in Fig. 6 in the top panel. The limit cycle may be periodic (seen as periodic window in the bifurcation structure) or quasi periodic depending on the parameter values. Both are shown in the bottom panel of Fig. 6.

Our main aim in this work is to identify the domain of chaos exactly in the parameter plane for the prey-predator model. Chaos occurs at critical points for the parameters a and d. We scan the parameter plane numerically increasing a and d in steps of 0.01 and undertake a dimensional

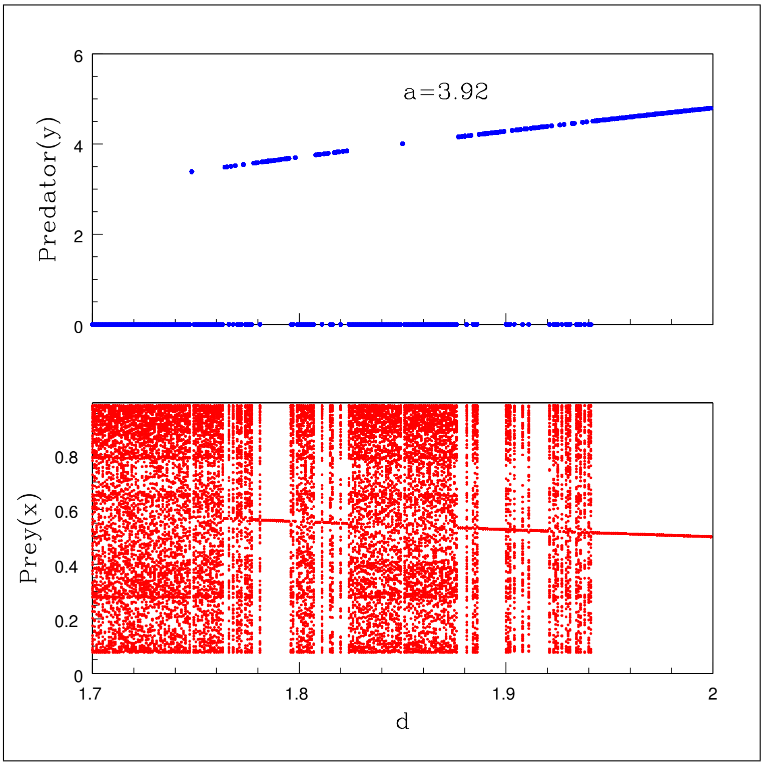

Figure 5. The top panel gives a magnified view of the small region between the two vertical lines in the previous figure. The lower panel shows the corresponding values of x for that region. Note that as y switches between 0 and a stable state, x switches between logistic chaos and a stable state.

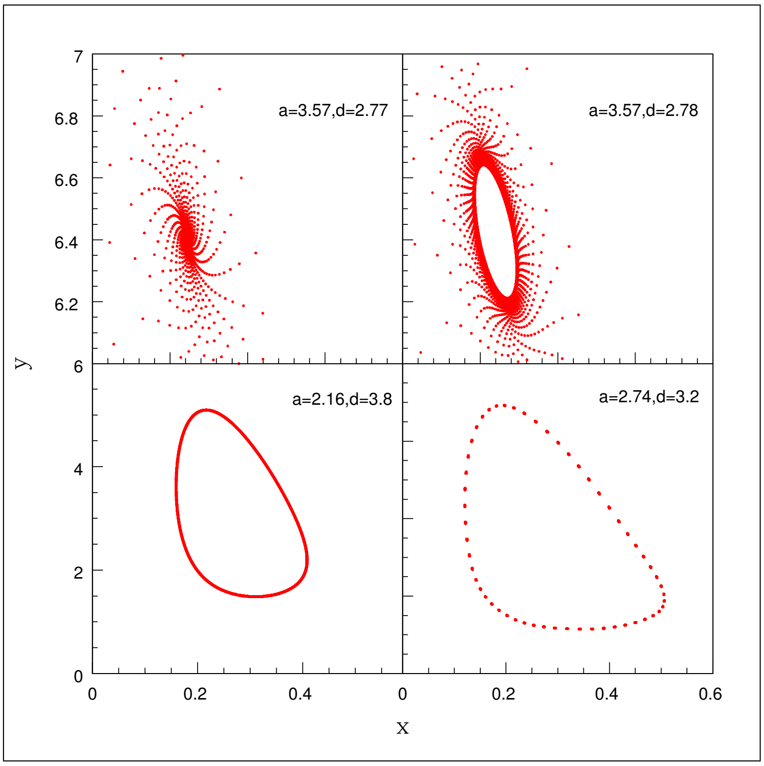

Figure 6. The top panel shows the nature of the attractor just before and after the Hopf bifurcation. The lower panel shows a quasi periodic limit cycle and a periodic window.

analysis to detect chaos. We use the modified box counting algorithm [12] to compute the correlation dimension D_2 by generating the time series. By using this scheme, we are able to locate the domain of chaos exactly in the parameter plane. In Fig. 7, we show the chaotic attractors for four different sets of parameter values (a, d). The corresponding D_2 values are shown in Fig. 8.

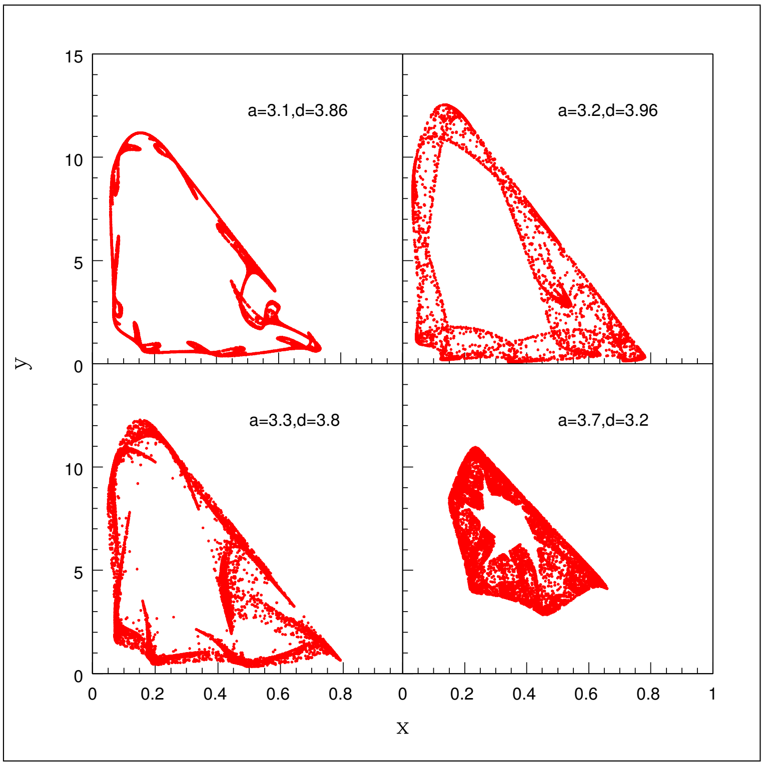

Figure 7. The chaotic attractors of the prey-predator model for four different parameter values.

To summarise, the different dynamical regimes of the prey-predator model obtained from our numerical analysis are shown in Fig. 9. The domain of chaos is denoted as region IV. The region (denoted as I) below the dashed line corresponds to extinction of predator and logistic dynamics for prey as a increases. The dotted line is the analytic curve (Eq.(5)) above which the second fixed point (x_2^*, y_2^*) should become stable. But numerically we find that the domain of extinction encroaches into the stable domain for lager a values. Thus, there is a region between the two lines (denoted V) where analytical and numerical results disagree and the predator is forced into extinction in competition with the prey. There is also a smaller region within this denoted by triangles, where the asymptotic state of the system depends sensitively on the parameter values.

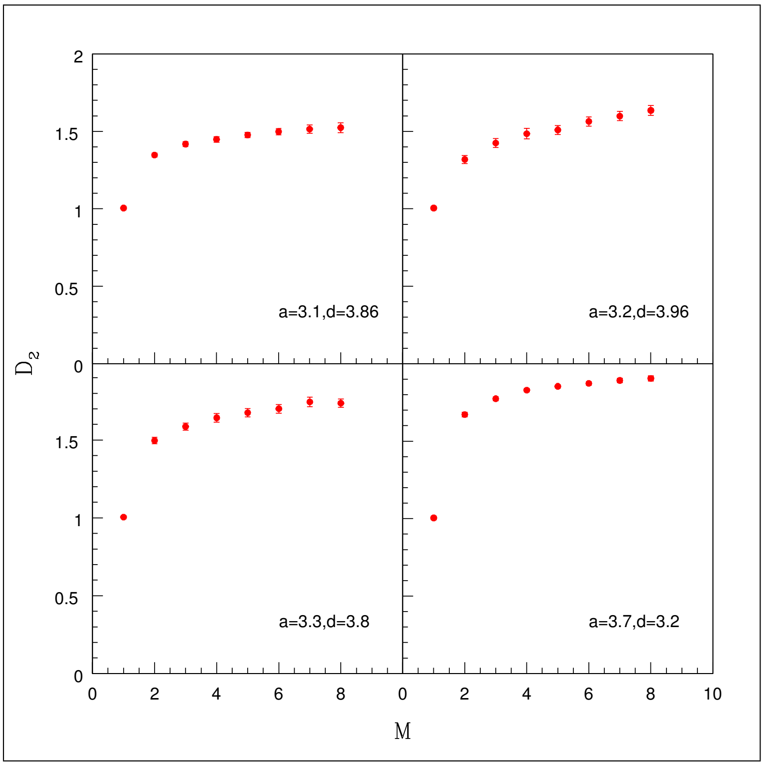

Figure 8. The correlation dimension D_2 of the four chaotic attractors in the previous figure as a function of the embedding dimension M.

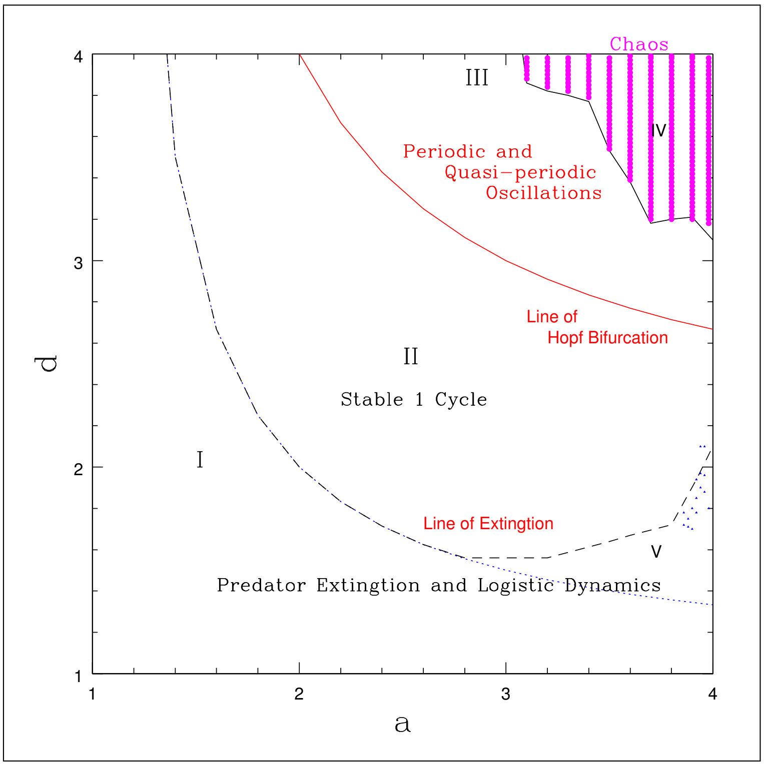

Figure 9. The complete parameter plane of the prey-predatoe model showing different domains of dynamics. The dotted line marks the stability of the second fixed point of the model. The dashed line which coincides with the dotted line for the major part, but bifurcates from it for larger a values represents the line of extinction of the predator. In the region below this line, denoted I, $y_n \rightarrow 0$ and the model displays logistic dynamics. The region II above this line represents the co-existence of predator and prey with stable one cycle. The solid line represents the transition from stable one cycle to periodic and quasi periodic oscillations by way of Hopf bifurcation. The region IV with solid vertical lines at the top right corner is where the dynamics turns chaotic. The region V where the dashed line bifurcates from the dotted line represents the competition between predator and prey and the predator is forced into extinction. There is a small part inside this, denoted by scattered triangles, where the asymptotic state of the system depends sensitively on the parameter values.

4. CONCLUSION

The prey-predator model is one of the most studied models in the context of deterministic chaos. Different versions of this model have been extensively studied by many authors in the past, both analytically and numerically. In this study, we numerically explore the parameter plane of the basic prey-predator model to identify various dynamical regimes, especially the chaotic regime. We are able to locate for the first time the exact domain of occurance of chaos in the parameter plane through a dimensional analysis. We compute the fractal dimension of the chaotic attractors for typical parameter values using a modified box counting scheme. Another interesting result we have obtained is the identification of a domain in the parameter plane where the asymptotic state deviates numerically from the analytically expected value and also a small region where the asymptotic state depends sensitively on the parameter values.

5. ACKNOWLEDGEMENTS

The work was done as part of the M. Sc project of PKT under the guidance of KPH. PKT acknowledges the support from the faculty and friends in the Department of Physics, The Cochin College.

References

[1] V. Voltera, *Opere Matematiche: Memorie e Note, Vol.5*, Acc. Naz. dei Lincei, Roma, 1962
[2] J. Hainzl, *SIAM J. Appl. Mathematics* **48**, 170(1988).
[3] X. He, *J. Mathematical Analysis & Applications* **198**, 355(1996).
[4] J. D. Murray, *Mathematical Biology*, (Springer, Berlin, 1998).
[5] R. M. May, *J. Theor. Biology* **51**, 511(1975).
[6] Z. J. Jing, Y. Chang and B. Guo, *Chaos, Solitons & Fractals* **21**, 701(2004).
[7] P. V. Ivanchikov and L. V. Nedorezov, *Comp. Ecology and Software* **1(2)**, 86(2011).
[8] A. A. Elsadany, *Comp. Ecology and Software* **2(2)**, 124(2012).
[9] Z. J. Jing and J. Yang, *Chaos, Solitons & Fractals* **27**, 259(2006).
[10] A. A. Elsadany, H. A. El-Metwally, E. M. Elabbasy and H. N. Agiza, *Comp. Ecology and Software* **2(3)**, 169(2012).
[11] M. Danca, S. Codreanu and B. Bako, *J. Biological Physics* **23**, 11(1997).
[12] K. P. Harikrishnan, R. Misra and G. Ambika, *Comm. Nonlinear Sci. Numer. Simulations* **17**, 263(2012).

Multiclass Classification of Cervical Cancer Tissues by Hidden Markov Model

Sabyasachi Mukhopadhyay[1], **Sanket Nandan**[1], **and Indrajit Kurmi**[2]
[1] Final Year, M.Sc., Indian Institute of Science Education and Research Kolkata.
[2] Final Year, M.Tech, Indian Institute of Technology Kanpur.

Abstract. In this paper, we report a hidden Markov model based multiclass classification of cervical cancer tissues. This model has been validated directly over time series generated by the medium refractive index fluctuations extracted from differential interference contrast images of healthy and different stages of cancer tissues. The method shows promising results for multiclass classification with higher accuracy.

Keywords. Differential Interference Contrast (DIC) images, Hidden Markov Model, Tissue Engineering.

1. INTRODUCTION

Cancer diagnosis through optical means is a hot area of current research. There are efficient signal processing tools like wavelets, multifractal detrended fluctuation analysis (MFDFA) which have shown promising outcomes in case of disease diagnosis [1,2,3,4]. We would like to note that these linear techniques are limited for binary classifications.

The current research works are more focused on probabilistic classifiers for extracting the hidden features in biological tissues and enhancing the accuracy of classification. The probabilistic classifiers like support vector machine (SVM), relevance vector machine (RVM), minimum distance classifier like Mahalanobis distance were found to have a lot of applications in biomedical domain for cancer diagnosis purpose [5-11]. In this paper, hidden Markov model (HMM), which is a dynamic Bayesian model, has been used for classifying cervical tissue samples of healthy and different stages of cancer.

2. THEORY

Suppose we have a non-empty finite element set of observation sequence, given by

$$O = (O_1, O_2, \ldots, O_\tau);$$

and Ω be the outcome (sample) space i.e. set of all possible outcomes or observations such that $\mid \Omega \mid > \infty$, thereby $O_t \in \Omega \forall t = 1, 2, \ldots, \pi$

Assume there exists some hidden state sequence, $\{X_t\}_{t=1,\ldots,\pi}$, which follows a Markov process, associated with the observation (data) sequence such that

$$X_t O = O_t \forall t; \text{ for some } O \tag{1}$$

Take $P = (P_{ij})_{n\times n}$ to be the transition probability matrix for the underlying Markov process with finite, discrete state space $X = \{1, 2, \ldots, n\}$; so that $p_{ij} := P(X_{t+1} = j \mid X_t = i)$

The structure of the matrix, O is given by, $O = \{o_j(k)\}_{n\times|\Omega|}$, commonly known as the observation probability matrix, such that $o_j(k) := P(O_t = k \mid X_t = j)$.

This model $\theta = (P, O, \pi)$, where π is the initial state (probability) distribution, is known as hidden Markov Model.

3. EXPERIMENTAL METHOD

The refractive index in space (two dimensional area of a tissue section) of the cervical tissue section with thickness $5\mu m$ and lateral dimension $\sim 4mm \times 6mm$, is the required stochastic (observed through measurement) variable for our study. The unstained tissue section has been concerned with the standard methods of tissue dehydration, thereafter embedding in wax, then sectioning under a rotary microtome and final dewaxing, performed on glass slides. The differential interference contrast (DIC) microscope (Olympus IX81, USA) measures the distribution of the refractive index on the section surface area of the tissue section. Separately, a CCD camera (ORCA-ERG, Hamamatsu) with pixel dimension $6.45\mu m$ and a point spread function microscope with width $\sim 0.36\mu m$ records the images of the stromal regions with 60X magnification. The multiclass classification has been performed over pixel-wise horizontally unfolded data. The DIC sample images are shown in Fig. 1. After unfolding the DIC images in a horizontal direction, it has been treated with Normal Testing method in the following ways.

1. Fluctuations= (Data-mean)/standard deviation
2. Computing the cumulative sum of fluctuations to generate the time series.

The above two steps are performed in order to process the medium refractive index fluctuations embedded in DIC images by HMM.

4. RESULTS AND DISCUSSIONS

Considering a tissue with potentially four different stages, namely, Grade I, II, III and normal (healthy), the horizontal surface of the plot has been partitioned into 44 rectangles, where prediction of each stages can lead to inaccurate detection of some other stage if there exists some non-zero percentage of detection in the off-diagonal rectangles given a particular stage to measure. The height or the perpendicular to the surface, z-axis displays the percentage of prediction of a given stage for the corresponding class (horizontal rectangles). The graph Fig. 2 shows clear distinction among the four different stages of the tissue. Data from normal cells are accurately predicted (with probability 1) as normal cells all the time creates a zero probability of false prediction in the rectangles (classes) of Grade I, II and III. The graph also shows that neither Grade I, nor II, nor III class is predicted as

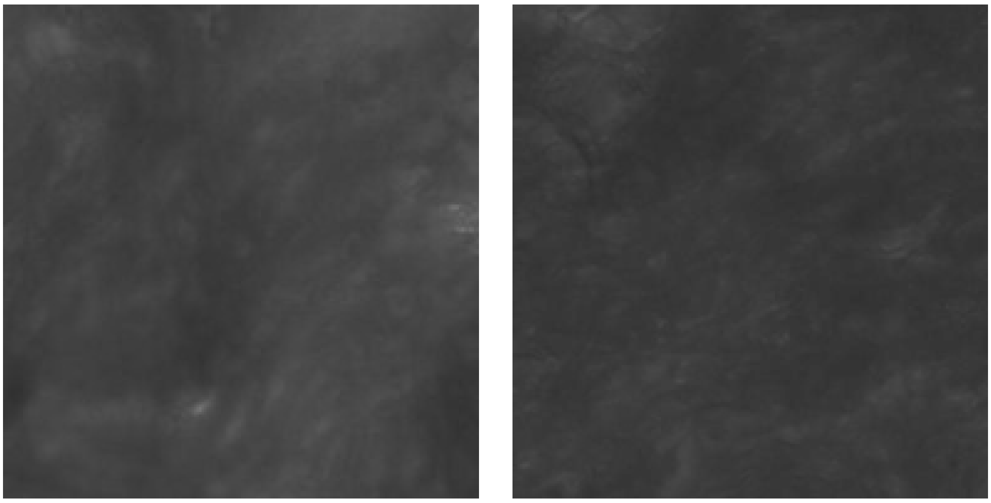

(a) Grade - I

(b) Grade - II

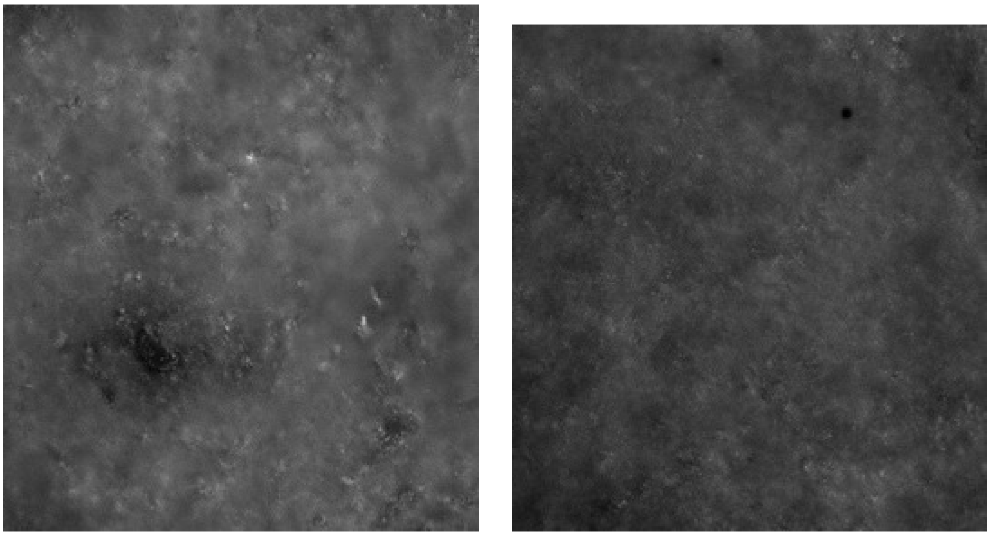

(c) Grade - III

(d) Normal

Figure 1. DIS images of different stages (Grade - I, II, III) of cancer and healthy (normal) tissues respectively

normal stage and hence it presents an advantage of classifying Grade I, II and III together, i.e., cancerous cells and normal cells. Similarly Grade I and II stages are also predicted in the correct class with 100% accuracy. But it is evident from the graph that there is an error in the correct prediction of Grade III stage. Grade III cells are correctly predicted with 97.34% accuracy and error in prediction of Grade III stage is 2.66% that falls in the class of Grade II. This error in prediction implies wrong prediction of a Grade III cell as Grade II cell with 2.66%, but the results never predict it as a Grade I or normal cell.

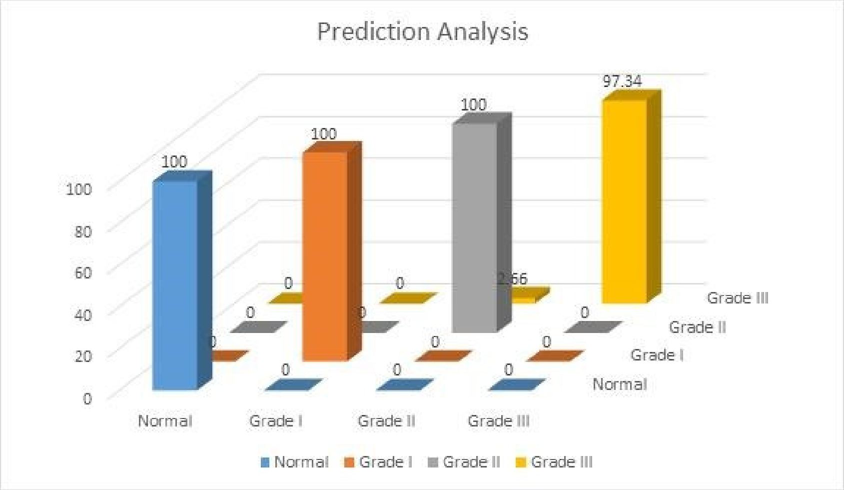

Figure 2. HMM based cervical tissue classification among healthy and different stages of cancer.

For the purpose of experimentation, we first train 17 model states in the hidden Markov model for each of the categories (stages). The training set for each category includes time series data obtained from experimentation. The model trained by the training data is defined as $\theta = (P, O,]\pi)$ with the state space $S = \{s_1, s_2, \ldots, s_{17}\}$. π deontes the prior probabilities, elements of P are the transition probabilities and elements of O denote the emission probabilities. Prior probabilities are first selected as a random function. P and O are modelled as Gaussian densities with mean 0 and variance 1. Then the data is trained on the model iteratively to fit and modify the model using EM (Expectation maximization) algorithm. The model is optimized using Lagrange multipliers. We use forward and backward algorithm to compute a set of sufficient statistics for our EM step tractably. Once the model is sufficiently trained for a given sequence of data we calculate the likelihood of sequence with model for each category, i.e., we calculate $P(\frac{X}{\theta_i})$ which is the sum of the joint likelihoods of the sequence over all possible state sequences allowed by the model for each category.

5. CONCLUSION

In conclusion, use of HMM has been found to be quite effective in multiclass classification purpose among the normal and different stages of cancer. Authors hope that the current study of HMM based application in DIC images of human cervical tissues will help the researchers to move this field forward.

ACKNOWLEDGMENT

The authors thank Dr. Asha Agarwal, G.S.V.M. Medical College and Hospital, Kanpur, for provision of the histopathologically characterized tissue samples.

References

[1] Alfano, R.R., Das,B.B., Cleary,J., Prudente,R., Celmer,E., ”Light sheds light on cancer distinguishing malignant tumors from benign tissues and tumors”, Bull. NY Acad. Med., 2nd Series, vol. 67, 1991, pp. 143-150 (1991).

[2] Mukhopadhyay, S., Das, N., Pradhan, A., Ghosh, N., Panigrahi, P.K., Pre-cancer Detection by Wavelet Transform and Multifractality in various Grades of DIC Stromal Images, SPIE Proceeding, SPIE BIOS, USA (2014).

[3] Mukhopadhyay, S., Das, N.K., Pradhan, A., Ghosh, N., Panigrahi, P.K., Wavelet and multi-fractal based analysis on DIC images in epithelium region to detect and diagnose the cancer progress among different Grades of tissues, SPIE Proceeding, SPIE Photonics Europe (2014).

[4] Mukhopadhyay, S., Mandal, S., Das, N.K., Dey, S., Mitra, A., Ghosh, N., Panigrahi, P.K., ”Diagnosing Heterogeneous Dynamics for CT Scan Images of Human Brain in Wavelet and MFDFA Domain”, Proceeding of Springer, IEM OPTRONIX-2014.

[5] Majumder, S.K., Ghosh, N., Gupta, P.K., ”Support vector machine for optical diagnosis of cancer,” J. Biomed. Opt. 10,024034 (2005).

[6] Majumder, S.K., Ghosh, N., Gupta, P.K., ”Relevance vector machine for optical diagnosis of cancer”, Lasers Surg. Med. 36, 323 (2005).

[7] Majumder, S.K., Kataria, S., Ghosh, N., Gupta, P.K., ”Nonlinear pattern recognition for laser induced fluorescence diagnosis of cancer”, Lasers Surg. Med. 33, 48 (2003).

[8] Devi, S., Panigrahi, P.K., Pradhan, A., ”Detecting cervical cancer progression through extracted intrinsic fluorescence and principal component analysis”, Journal of biomedical optics 19 (12), 127003-127003 (2014).

[9] Baum, L. E., Petrie, T., ”Statistical Inference for Probabilistic Functions of Finite State Markov Chains”. The Annals of Mathematical Statistics 37 (6) (1966).

[10] Mukhopadhyay,S., Ghosh,N., Barman,R., Panigrahi,P.K., Pratiher,S., Pradhan,A., S-TRANSFORM BASED FLUCTUATION ANALYSIS- A METHOD FOR PRECANCER DETECTION, IEEE Proceeding, Microcom-2016, India.

[11] Mukhopadhyay,S., Kurmi,I., Dey,R., Das,N.K., Pradhan,S.,Pradhan,A., Ghosh,N., Panigrahi,P.K., Mo-

hanty,S., Optical diagnosis of colon and cervical cancer by support vector machine, SPIE Proceeding, SPIE Photonics Europe, Belgium, 2016, Europe.

STUDENT JOURNAL OF PHYSICS

Volume 6 **Number 1** **March 2017**

CONTENTS

ARTICLES